PHOTONICS Research

Submegahertz spectral width photon pair source based on fused silica microspheres

Erasto Ortiz-Ricardo,[1] Cesar Bertoni-Ocampo,[1] Mónica Maldonado-Terrón,[1] Arturo Garcia Zurita,[1] Roberto Ramirez-Alarcon,[2] Hector Cruz Ramirez,[1] R. Castro-Beltrán,[3,4] and Alfred B. U'Ren[1,*]

[1]Instituto de Ciencias Nucleares, Universidad Nacional Autónoma de México, Apartado Postal 70-543, 04510 México, D.F., Mexico
[2]Centro de Investigaciones en Óptica A.C., Loma del Bosque 115, Colonia Lomas del Campestre, 37150 León, Guanajuato, Mexico
[3]Departamento de Ingeniería Física, Cuerpo Académico de Mécanica Estadística, Divisón de Ciencias e Ingenierías, Universidad de Guanajuato, 37150 León, Guanajuato, Mexico
[4]e-mail: cbrigoberto@fisica.ugto.mx
*Corresponding author: alfred.uren@correo.nucleares.unam.mx

Received 30 June 2021; revised 30 August 2021; accepted 1 September 2021; posted 1 September 2021 (Doc. ID 435521); published 21 October 2021

High-efficiency submegahertz bandwidth photon pair generators will enable the field of quantum technology to transition from laboratory demonstrations to transformational applications involving information transfer from photons to atoms. While spontaneous parametric processes are able to achieve high-efficiency photon pair generation, the spectral bandwidth tends to be relatively large, as defined by phase-matching constraints. To solve this fundamental limitation, we use an ultrahigh quality factor (Q) fused silica microsphere resonant cavity to form a photon pair generator. We present the full theory for the spontaneous four-wave mixing (SFWM) process in these devices, fully taking into account all relevant source characteristics in our experiments. The exceptionally narrow (down to kilohertz-scale) linewidths of these devices result in a reduction in the bandwidth of the photon pair generation, allowing submegahertz spectral bandwidth to be achieved. Specifically, using a pump source centered around 1550 nm, photon pairs with the signal and idler modes at wavelengths close to 1540 and 1560 nm, respectively, are demonstrated. We herald a single idler-mode photon by detecting the corresponding signal photon, filtered via transmission through a wavelength division multiplexing channel of choice. We demonstrate the extraction of the spectral profile of a single peak in the single-photon frequency comb from a measurement of the signal–idler time of emission distribution. These improvements in device design and experimental methods enabled the narrowest spectral width ($\Delta\nu = 366$ kHz) to date in a heralded single-photon source based on SFWM.

https://doi.org/10.1364/PRJ.435521

1. INTRODUCTION

Advances in quantum technologies over the past two decades have made possible an exciting breadth of applications in fields such as communications [1], imaging [2], and computation [3]. Photon pair generation based on the spontaneous parametric downconversion (SPDC) [4] and four-wave mixing [5] processes has played an essential role in this revolution due to the ease with which the quantum entanglement characteristics of the emitted signal and idler photons may be tailored, and on account of their ability to propagate long distances either in free space or in optical fibers, with minimal interaction with the environment. However, a number of key challenges must be overcome in order for photon pair generation technology to achieve its true potential, including: (i) source miniaturization, enabling the eventual on-chip integration of source, optical manipulation, and detection [6,7]; (ii) increasing the conversion efficiency, thus permitting high-brightness photon pair emission with the lowest possible pump power; (iii) photon pair indistinguishability, including spectral factorizability, permitting photons from distinct sources to interfere [8]; and (iv) the reduction of the emission bandwidth to the megahertz, or submegahertz, level so as to be compatible with atomic electronic transitions [9]. The last requirement must be achieved in order to create single atom–single photon interfaces that will facilitate information transfer from photons, in the form of flying qubits, to atoms, thus constituting a quantum memory. This technology is essential for the further progress of quantum information processing based on photons.

An optical platform that has the potential to simultaneously meet all of these requirements is the ultrahigh Q optical

microresonator. As a result of the long photon lifetimes inside the cavities, extremely high circulating intensities are possible, resulting in very low optical thresholds for nonlinear behaviors [10–12]. In addition, the extremely narrowband resonances lead to nonlinear optical effects occurring at very well-defined frequencies. Because cavity-enhanced photon pair generation involves emission in well-defined cavity modes, by isolating a single cavity resonance for each of the signal and idler modes, the resulting two-photon state ends up being naturally spectrally factorizable, ensuring indistinguishability [13]. Lastly, microresonators are uniquely well positioned to permit source integration [14,15].

There are two possible routes for generating photon pairs based on spontaneous parametric processes that can occur in microresonators: the SPDC process based on second-order nonlinear materials [16–21], and the spontaneous four-wave mixing (SFWM) process based on third-order nonlinear materials [22–29]. Photon pair generation from a cavity-enhanced source, in which the nonlinear medium is contained by an optical cavity, based on either of these two processes with a narrowband pump, leads to a joint spectral amplitude in the form of a frequency comb expressed as a function of the frequency difference $\omega_s - \omega_i$, in terms of the signal ω_s and idler ω_i frequencies. While each resulting comb peak has a width that is inversely proportional to the cavity quality factor Q, the intrapeak separation [or free spectral range (FSR)] is inversely proportional to the cavity round-trip time [13,30]. Thus, an important benefit of a microresonator as compared to an extended cavity design is that the comb peaks end up being separated by a greater spectral distance, facilitating the possibility of addressing individual comb peaks. Note that in the classical nonlinear optics realm, four-wave mixing in optical resonators is likewise known to naturally give rise to the emission of frequency combs, with applications in the field of atomic clocks and generally in metrology [31,32].

Note that in the standard SPDC and SFWM processes (without the use of optical cavities), the spread of emission frequencies is limited mainly by phase-matching constraints and can be substantial. Such large bandwidths are useful in certain situations, e.g., they lead to narrow Hong–Ou–Mandel interference dips, which in turn permit a large resolution in quantum optical coherence tomography devices [33,34]. However, as already mentioned, the basic requirement for the development of single atom–single photon interfaces is the emission of narrowband photon pairs [35–37].

Cavity-enhanced SPDC sources have been demonstrated using integrated microresonators [17,19], nonlinear waveguide cavities [21], and free-space extended cavities [20,38–41]. In the case of SFWM, cavity-enhanced photon pair sources have likewise been based on microring [14,15,24,25,27–29,42] and microdisk [43] cavities. In this paper, we report the first demonstration of a photon pair source based on fused silica microspheres and present a theory for SFWM in these devices that leads to simulations that agree well with our measurements. In this work, we extend our previous cavity-enhanced SFWM theory [13], so as to include important characteristics relevant to our current experimental results such as: (i) all four waves at resonance in the cavity; (ii) pump varied in time to maintain resonance, leading to two-photon state in the form of a statistical mixture; and (iii) analysis carried out for micro- rather than extended cavities. Here we report ultranarrow photon pair generation, with emission bandwidths down to $\Delta\nu = 366$ kHz. While this small single-photon bandwidth is similar to those observed in certain extended-cavity SPDC sources (e.g., 666 kHz in Ref. [38] and 265 kHz in Ref. [9]), it represents an ∼43× improvement with respect to the previously reported spectrally narrowest SFWM source (15.9 MHz) [44].

2. THEORY FOR THE SFWM PROCESS IN MICROSPHERES

Here we are interested in studying photon pairs produced by SFWM in a fused silica microsphere, with radius R, as the nonlinear medium. The pump is assumed to be coupled evanescently from an elongated (tapered) fiber to a mode circulating on the sphere's equator; see, for example, Ref. [45]. Photon pairs produced in the sphere can then couple out back to the tapered fiber, whence they may be directed as desired to an experiment of interest; see Fig. 1.

Each of the four waves participating in the SFWM process is assumed to propagate along the equator on the plane $\theta = \pi/2$, parallel to the unit vector $\vec{e}_\phi$. Expressed in spherical coordinates, the Hamiltonian for this process may be written as

$$\hat{H}(t) = \frac{3}{4}\epsilon_0\chi^{(3)}\int_0^{2\pi}\mathrm{d}\phi\int_0^{\pi}\mathrm{d}\theta\int_0^{R}\mathrm{d}\rho\rho^2\sin\theta E_1^{(+)}(\vec{r},t)E_2^{(+)}(\vec{r},t) \times\hat{E}_s^{(-)}(\vec{r},t)\hat{E}_i^{(-)}(\vec{r},t) + \mathrm{H.C.}, \quad (1)$$

in terms of the third-order optical nonlinearity $\chi^{(3)}$, the permittivity of free-space ϵ_0, the positive frequency electric field operators for each of the two pumps $E_1^{(+)}(\vec{r},t)$ and $E_2^{(+)}(\vec{r},t)$, and the negative frequency electric field operators for the signal and the idler, $\hat{E}_s^{(-)}(\vec{r},t)$ and $\hat{E}_i^{(-)}(\vec{r},t)$.

We describe each mode supported by the sphere by an index vector $\vec{l}$ composed of the l, m, and q individual indices related to azimuthal, polar, and radial coordinates, respectively. Each of the pump waves ($\nu = 1$ and $\nu = 2$), traveling in modes $\vec{l}_1$ and $\vec{l}_2$, respectively, is described classically as

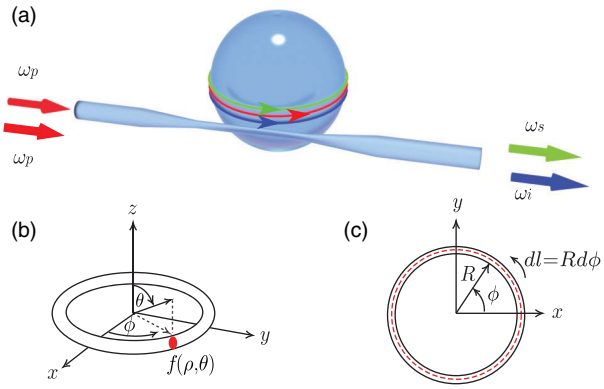

Fig. 1. (a) Schematic of an SFWM photon pair source based on a fused silica microsphere, evanescently coupled to a fiber taper placed in closed proximity; (b) transverse mode of propagation around the sphere perimeter; (c) top view of the guided mode.

$$E_\nu^{(+)}(\vec{r},t)=\sum_{\vec{l}_\nu}A_{\vec{l}_\nu}f_{\vec{l}_\nu}(\rho,\theta)\int \mathrm{d}\omega\alpha_{\vec{l}_\nu}(\omega)e^{-i[\omega t-k_{\vec{l}_\nu}(\omega)R\phi]}, \quad (2)$$

where $A_{\vec{l}_\nu}$ is the amplitude, $f_{\vec{l}_\nu}(\rho,\theta)$ is the transverse field distribution (for a fixed value of ϕ), and $\alpha_{\vec{l}_\nu}(\omega)$ is the spectral envelope for each of the two pump waves, $\nu=1$ and $\nu=2$. The electric field for the signal and idler photons is described quantum mechanically as follows:

$$\hat{E}_\nu^{(+)}(\vec{r},t)=\sum_{\vec{l}_\nu}f_{\vec{l}_\nu}(\rho,\theta)\int \mathrm{d}\omega\ell(\omega)e^{-i[\omega t-k_{\vec{l}_\nu}(\omega)R\phi]}\hat{b}_{\vec{l}_\nu}(k_\omega), \quad (3)$$

where $\hat{b}_{\vec{l}_\nu}(k_\omega)$ is the annihilation operator for mode $\vec{l}_\nu$, for each of the signal ($\nu=s$) and idler ($\nu=i$); $f_{\vec{l}_\nu}(\rho,\theta)$ represents the signal and idler transverse spatial distributions; and the function $\ell(\omega)$ is given as $\ell(\omega)=\omega^{1/2}/[n(\omega)v_g(\omega)]$, with $n(\omega)$ and $v_g(\omega)$ the refractive index and the group velocity, respectively.

The resonant wavelengths in the sphere can be obtained solving numerically the following equation, derived from a Mie scattering approach, for λ (for particular values of the indices azimuthal l, polar m, and radial q) [46]:

$$\frac{1}{\lambda}=\frac{1}{2\pi Rn_s(\lambda)}\left\{\nu+2^{-\frac{1}{3}}\alpha_q\nu^{\frac{1}{3}}-\frac{P(\lambda)}{[n_s(\lambda)^2-1]^{\frac{1}{2}}}+\frac{3}{10}2^{-\frac{2}{3}}\alpha_q^2\nu^{-\frac{1}{3}}-\frac{2^{-\frac{1}{3}}P(\lambda)[n_s(\lambda)^2-\frac{2}{3}P(\lambda)^2]}{[n_s^2(\lambda)-1]^{\frac{3}{2}}}\alpha_q\nu^{-\frac{2}{3}}\right\}, \quad (4)$$

where R is the sphere radius, $P(\lambda)=n_s(\lambda)$ for a TE mode, and $P(\lambda)=1/n_s(\lambda)$ for a TM mode, with $n_s(\lambda)$ the fused silica index of refraction obtained from the Sellmeier equation [47]. In Eq. (4), $\nu=l+1/2$ and α_q represents the zeros of the Airy function $\mathrm{Ai}(-z)$; for simplicity, in this work we have considered only modes with $l=\mathrm{m}$ and $q=1$, so that $\vec{l}=(l,\mathrm{m},q)$ reduces to $(l,l,1)$. We can obtain the effective index for each whispering gallery mode $n_{\mathrm{eff}}(\lambda)$, with help of the resonance condition, as $n_{\mathrm{eff}}(\lambda)=l\lambda/L$, with $L=2\pi R$. The dispersion relation is subsequently obtained as $k(\omega)=n_{\mathrm{eff}}(\omega)\omega/c$.

The quantum state is then obtained, following a standard perturbative approach, as

$$|\Psi\rangle\approx|0\rangle+\frac{1}{i\hbar}\int_0^t \mathrm{d}t'\hat{H}(t')|0\rangle. \quad (5)$$

Replacing the expressions for the electric field [Eqs. (2) and (3)] into the Hamiltonian Eq. (1), we obtain the quantum state $|\Psi\rangle=|0\rangle+\eta|\Psi_2\rangle$, written in terms of a constant related to the source brightness η and the two-photon component of the state $|\Psi_2\rangle$, the latter given by

$$\begin{aligned}|\Psi_2\rangle&=\frac{1}{i\hbar}\int_0^t \mathrm{d}t'\hat{H}(t')|0\rangle\\&=\sum_{\vec{l}_1,\vec{l}_2,\vec{l}_s,\vec{l}_i}A_{\vec{l}_1}A_{\vec{l}_2}\Theta_{\vec{l}_1\vec{l}_2\vec{l}_s\vec{l}_i}\int \mathrm{d}\omega_s\int \mathrm{d}\omega_i\left\{l(\omega_s)l(\omega_i)\right.\\&\quad\times\int \mathrm{d}\omega_1\left[\alpha_{\vec{l}_1}(\omega_1)\alpha_{\vec{l}_2}(\omega_s+\omega_i-\omega_1)G_{\vec{l}_1\vec{l}_2\vec{l}_s\vec{l}_i}(\omega_1,\omega_s,\omega_i)\right.\\&\quad\left.\left.\times\hat{b}_{\vec{l}_s}^\dagger(\omega_s)\hat{b}_{\vec{l}_i}^\dagger(\omega_i)|0\rangle\right]\right\}. \quad (6)\end{aligned}$$

Here we have assumed that the time interval between photon pair emission events is much greater than the characteristic time for each event, so that the limits of the temporal integral may be extended to $\pm\infty$. Note that in writing this expression for $|\Psi_2\rangle$, we have defined the field overlap $\Theta_{\vec{l}_1\vec{l}_2\vec{l}_s\vec{l}_i}$, given by

$$\Theta_{\vec{l}_1\vec{l}_2\vec{l}_s\vec{l}_i}=\int \mathrm{d}\rho\int \mathrm{d}\theta\rho^2\sin\theta f_1(\rho,\theta)f_2(\rho,\theta)f_s^*(\rho,\theta)f_i^*(\rho,\theta), \quad (7)$$

and the function $G_{\vec{l}_1\vec{l}_2\vec{l}_s\vec{l}_i}(\omega_1,\omega_s,\omega_i)$ expressed in terms of the sphere's equatorial perimeter $L=2\pi R$, as

$$G_{\vec{l}_1\vec{l}_2\vec{l}_s\vec{l}_i}(\omega_1,\omega_s,\omega_i)=\mathrm{sinc}\left[\frac{L\Delta k_{\vec{l}_1\vec{l}_2\vec{l}_s\vec{l}_i}(\omega_1,\omega_s,\omega_i)}{2}\right]\times\exp\left[i\frac{L\Delta k_{\vec{l}_1\vec{l}_2\vec{l}_s\vec{l}_i}(\omega_1,\omega_s,\omega_i)}{2}\right], \quad (8)$$

defined in turn in terms of the phase mismatch function,

$$\Delta k_{\vec{l}_1\vec{l}_2\vec{l}_s\vec{l}_i}(\omega_1,\omega_s,\omega_i)=k_{\vec{l}_1}(\omega_1)+k_{\vec{l}_2}(\omega_s+\omega_i-\omega_1)-k_{\vec{l}_s}(\omega_s)-k_{\vec{l}_i}(\omega_i). \quad (9)$$

Let us now assume that the two pumps are degenerate (spatially and spectrally), as well as monochromatic at frequency ω_p, i.e.,

$$\alpha_{\vec{l}_p}(\omega)\equiv\alpha_{\vec{l}_1}(\omega)=\alpha_{\vec{l}_2}(\omega)=\delta(\omega-\omega_p). \quad (10)$$

Let us consider a short longitudinal section of the continuous-wave pump of length Δz_p (with $\Delta z_p\ll L$). Performing the change of variables $\Omega=\omega_s-\omega_p$, we then obtain the state resulting from one cavity round trip of this longitudinal pump section of Δz_p length

$$\begin{aligned}|\Psi_2\rangle&=\sum_{\vec{l}_p,\vec{l}_s,\vec{l}_i}A_{\vec{l}_p}^2\Theta_{\vec{l}_p\vec{l}_p\vec{l}_s\vec{l}_i}\int \mathrm{d}\Omega\ell(\omega_p+\Omega)\ell(\omega_p-\Omega)\\&\quad\times g_{\vec{l}_p\vec{l}_s\vec{l}_i}(\Omega)\hat{b}_{\vec{l}_s}^\dagger(\omega_p+\Omega)\hat{b}_{\vec{l}_s}^\dagger(\omega_p-\Omega)|0\rangle, \quad (11)\end{aligned}$$

where the function $g_{\vec{l}_p\vec{l}_s\vec{l}_i}(\Omega)$, which constitutes a reduced version of $G_{\vec{l}_1\vec{l}_2\vec{l}_s\vec{l}_i}(\omega_1,\omega_s,\omega_i)$, can be expressed as

$$g_{\vec{l}_p\vec{l}_s\vec{l}_i}(\omega_p,\Omega)=\mathrm{sinc}\left[\frac{L\Delta\kappa_{\vec{l}_p\vec{l}_s\vec{l}_i}(\omega_p,\Omega)}{2}\right]\exp\left[i\frac{L\Delta\kappa_{\vec{l}_p\vec{l}_s\vec{l}_i}(\omega_p,\Omega)}{2}\right] \quad (12)$$

in terms of the reduced phase mismatch function,

$$\Delta\kappa_{\vec{l}_p\vec{l}_s\vec{l}_i}(\omega_p,\Omega)=2k_{\vec{l}_p}(\omega_p)-k_{\vec{l}_s}(\omega_p+\Omega)-k_{\vec{l}_i}(\omega_p-\Omega)-2\gamma P. \quad (13)$$

Note that in the above expression, we have incorporated a nonlinear term in the phase mismatch associated with self- and cross-phase modulation $2\gamma P$ [47]. This term can be written in terms of the Q parameter of the cavity, of the input power P_{in}, of the nonlinear index of refraction n_2, and of the effective transverse mode area A_{eff} as

$$2\gamma P = \frac{P_{\text{in}} Q n_2}{\pi n R A_{\text{eff}}}. \tag{14}$$

Using the fact that the function $\ell(\omega)$ is a slow function of ω, and assuming that each of the three waves (the degenerate pump, signal, and idler) travels in a single spatial mode, the quantum state can be simplified as $|\Psi\rangle = |0\rangle + \eta'|\Psi_2\rangle$, where the new constant η' incorporates the quantity $A_{\vec{l}_p}^2 \Theta_{\vec{l}_p\vec{l}_p\vec{l}_s\vec{l}_i}$, with $|\Psi_2\rangle$ given by

$$|\Psi_2\rangle = \int \mathrm{d}\Omega g_{\vec{l}_p\vec{l}_s\vec{l}_i}(\Omega)\hat{b}_{\vec{l}_s}^{\dagger}(\omega_p+\Omega)\hat{b}_{\vec{l}_s}^{\dagger}(\omega_p-\Omega)|\text{vac}\rangle. \tag{15}$$

So far, the quantum state has been expressed in terms of the annihilation operators $\hat{b}_{\vec{l}_s}$ and $\hat{b}_{\vec{l}_i}$, which correspond to the modes resonating within the sphere. In any realistic experiment, we of course need to couple the photon pairs out of the resonating sphere so as to use them in an experimental setup of interest. This can be accomplished through evanescent coupling of the sphere modes to a given propagation mode of a tapered fiber placed in close proximity to the sphere. Let us denote as $\hat{a}_\nu$ the extracavity mode in the tapered fiber (we assume that light couples into a single taper mode) for the signal ($\nu = s$) and idler ($\nu = i$), with r_ν representing the reflectivity of the sphere–taper interface (the probability amplitude corresponding to a photon remaining within the sphere), and t'_ν representing the transmissivity (the probability amplitude corresponding to a photon coupling from the sphere to the taper); in a lossless cavity, energy conservation dictates $|t'_\nu|^2 + |r_\nu|^2 = 1$, with $|r_\nu| = 1 - \frac{l\pi}{Q}$. After $n+1$ iterations in the cavity the intracavity mode $\hat{b}_{\vec{l}_s}$ and $\hat{b}_{\vec{l}_i}$ can be expressed as follows:

$$\hat{b}_{\vec{l}_\nu}^{\dagger}(\omega) \to r_\nu^{n+1} + e^{\text{ink}_{\vec{l}_\nu}}(\omega)L\,\hat{a}_\nu^{\dagger}(\omega) + \left[\frac{1 - r_\nu^{n+1} e^{i(n+1)k_{\vec{l}_\nu(\omega)}L}}{1 - r_\nu e^{ik_{\vec{l}_\nu}(\omega)}L}\right] t'_\nu \hat{a}_\nu^{\dagger}(\omega). \tag{16}$$

Taking the limit $n \to \infty$, so that all SFWM light produced by a single cavity round trip of the longitudinal pump section of length Δz_p is allowed to escape the cavity, we may write the extracavity mode operator as follows:

$$\lim_{n\to\infty} \hat{b}_{\vec{l}_\nu}^{\dagger}(\omega)|0\rangle_\nu = A_\nu(\omega)\hat{a}_\nu^{\dagger}(\omega)|0\rangle_\nu, \tag{17}$$

written in terms of the Airy function $A_\nu(\omega)$,

$$A_\nu(\omega) = \frac{t'_\nu}{1 - r_\nu e^{ik_{\vec{l}_\nu}(\omega)L}}. \tag{18}$$

We may then write the two-photon state propagating in the tapered fiber modes $|\Psi'_2\rangle$, described by annihilation operators $\hat{a}_s$ and $\hat{a}_i$, as

$$|\Psi'_2\rangle = \int \mathrm{d}\Omega g_{\vec{l}_p\vec{l}_s\vec{l}_i}(\Omega)A_s(\omega_p+\Omega)A_i(\omega_p-\Omega) \times \hat{a}_s^{\dagger}(\omega_p+\Omega)\hat{a}_i^{\dagger}(\omega_p-\Omega)|0\rangle. \tag{19}$$

Let us note that this is the quantum state produced by a single pass of the pump field through the cavity. In an experimental situation of interest, the pump field is resonant in the cavity, so that with a probability amplitude t each pump photon couples from the taper to the sphere, and once within the cavity it remains with a probability amplitude r_p at each pass through the taper–sphere interface. We can then write an expression for the two-photon state $|\Psi''_2\rangle$, resulting from n iterations of the pump in the cavity,

$$\begin{aligned}|\Psi''_2\rangle &= t_p|\Psi'_2\rangle + t_p r_p^2 e^{ik_{\vec{l}_p}(\omega_p)L}|\Psi'_2\rangle + t_p r_p^4 e^{i2k_{\vec{l}_p}(\omega_p)L}|\Psi'_2\rangle \\ &\quad + \ldots + t_p r_p^{2n} e^{i2nk_{\vec{l}_p}(\omega_p)L}|\Psi'_2\rangle \\ &= \frac{t_p[1 - r_p^{2(n+1)} e^{ik_{\vec{l}_p}(\omega_p)L(n+1)}]}{1 - r_p^2 e^{ik_{\vec{l}_p}(\omega_p)L}}|\Psi'_2\rangle.\end{aligned} \tag{20}$$

In this expression, upon each successive round trip of the pump longitudinal section Δz_p in the cavity, the electric-field amplitudes $A_{\vec{l}_1}$ and $A_{\vec{l}_2}$ are each reduced by r_p, so that a factor r_p^2 appears in addition to the phase term corresponding to one round trip for each pump (both from a single degenerate pump mode). In the limit $n \to \infty$ corresponding to a situation in which all the pump light from longitudinal section Δz_p initially coupled into the cavity has escaped, we may then write the resulting two-photon state $|\Psi''_2\rangle$ as follows:

$$\lim_{n\to\infty}|\Psi''\rangle = A_p(\omega_p)|\Psi'\rangle \tag{21}$$

in terms of the Airy function for the pump $A_p(\omega)$, expressed as

$$A_p(\omega) = \frac{t_p}{1 - r_p^2 e^{ik_{\vec{l}_p}(\omega)L}}. \tag{22}$$

We can then write the two-photon state, which incorporates the full effect of the cavity, as follows (note that the derivation shown here pertains to the case of degenerate pump waves; in the case of nondegenerate pumps, spatially and/or spectrally, two separate Airy functions will appear, one for each of the pumps):

$$\begin{aligned}|\Psi''(\omega_p)\rangle &= |\text{vac}\rangle + \eta' A_p(\omega_p) \times \int \mathrm{d}\Omega f(\Omega;\omega_p)\hat{a}_s^{\dagger}(\omega_p+\Omega)\hat{a}_i^{\dagger}(\omega_p-\Omega)|\text{vac}\rangle \\ &\equiv |\text{vac}\rangle + \eta' A_p(\omega_p)|\varphi(\omega_p)\rangle,\end{aligned} \tag{23}$$

in terms of the joint spectral amplitude function $f(\Omega;\omega_p)$,

$$f(\Omega;\omega_p) = g_{\vec{l}_p\vec{l}_s\vec{l}_i}(\Omega;\omega_p)A_s(\omega_p+\Omega)A_i(\omega_p-\Omega). \tag{24}$$

Alternatively, it is useful for visualization purposes to write the two-photon state in an equivalent form involving the two-dimensional frequency generation space $\{\omega_s, \omega_i\}$, as follows:

$$|\Psi''(\omega_p)\rangle = |\text{vac}\rangle + \eta' A_p(\omega_p) \times \int \mathrm{d}\omega_s \int \mathrm{d}\omega_i f_2(\omega_s,\omega_i;\omega_p)\hat{a}_s^{\dagger}(\omega_s)\hat{a}_i^{\dagger}(\omega_i)|\text{vac}\rangle \tag{25}$$

in terms of the two-dimensional joint spectral amplitude,

$$f_2(\omega_s,\omega_i;\omega_p) = \delta(\omega_s+\omega_i-2\omega_p)G_{\vec{l}_p\vec{l}_p\vec{l}_s\vec{l}_i}(\omega_p,\omega_s,\omega_i)A_s(\omega_s)A_i(\omega_i). \tag{26}$$

It is convenient to re-express this joint amplitude in terms of "rotated" variables, $\Omega = (\omega_s - \omega_i)/2$ (already introduced) and $\omega_+ = (\omega_s + \omega_i)/2$ as

$$f_2'(\omega_+,\Omega;\omega_p)=\delta(\omega_+-\omega_p)\times G_{\vec{l}_p\vec{l}_p\vec{l}_s\vec{l}_i}(\omega_p,\omega_++\Omega,\omega_+-\Omega)\times A_s(\omega_++\Omega)A_i(\omega_+-\Omega). \quad (27)$$

In our experiments, while the pump wave is in the form of a continuous wave with a narrowband linewidth δ_p, the pump frequency is varied in time according to a triangular wave with amplitude Δ_p and frequency f_p. As ω_p is swept within the spectral window of width Δ_p, a bandwidth Δ_r corresponding to the spectral width of the cavity resonance function $|A_p(\omega_p)|^2$ can couple into the cavity. There are therefore three bandwidths of interest that govern the pump and its interaction with the cavity: (i) pump linewidth δ_p, (ii) pump resonance bandwidth Δ_p, and (iii) pump sweeping range Δ_r. In our experiments (see below) the relationships $\delta_p \ll \Delta_p \ll \Delta_r$ are fulfilled with approximate values $\delta_p \approx 200$ kHz, $\Delta_p \approx 20$ MHz, and $\Delta_r \approx 25$ GHz.

Let us now express the two-photon state produced by the sphere as a statistical mixture of all the pure states produced by each individual pump spectral component ω_p that can couple into the sphere, as follows:

$$\hat{\rho}=\int d\omega_p |A_p(\omega_p)|^2 |\varphi(\omega_p)\rangle\langle\varphi(\omega_p)|. \quad (28)$$

We can now write down an expression for the spectral intensity (SI) for the idler photon $R_i(\Omega)$, in terms of the photon number operators $\hat{n}(\omega_\nu)=a^\dagger(\omega_\nu)a(\omega_\nu)$ (with $\nu=s,i$), as follows:

$$R_i(\Omega)=\int d\omega_s\langle\hat{n}(\omega_s)\hat{n}(\omega_p-\Omega)\rangle \quad (29)$$

$$=\mathrm{Tr}[\hat{a}^\dagger(\omega_s)\hat{a}^\dagger(\omega_p-\Omega)\hat{a}(\omega_p-\Omega)\hat{a}(\omega_s)\hat{\rho}]$$

$$=\int d\omega_p |A(\omega_p)f(\Omega;\omega_p)|^2. \quad (30)$$

An explicit version of the above equation is as follows, where in the second line we have used the approximation that the state is defined by the three Airy functions with a negligible effect of the phase-matching function:

$$R_i(\Omega)=\int d\omega_p |g_{\vec{l}_p\vec{l}_s\vec{l}_i}(\Omega)|^2 \mathcal{A}_p(\omega_p)\mathcal{A}_s(\omega_p+\Omega)\mathcal{A}_i(\omega_p-\Omega)$$

$$\approx\int d\omega_p \mathcal{A}_p(\omega_p)\mathcal{A}_s(\omega_p+\Omega)\mathcal{A}_i(\omega_p-\Omega) \quad (31)$$

in terms of the intensity Airy functions $\mathcal{A}_\nu(\omega)\equiv|A_\nu(\omega)|^2$ (with $\nu=p,s,i$). It is of interest to write equivalent expressions in time domain, for which we define time-domain annihilation operators as follows:

$$\hat{a}_t(t)=\frac{1}{2\pi}\int d\omega \hat{a}(\omega)e^{-i\omega t}. \quad (32)$$

We can then write down an expression for the resulting two-photon times of emission distribution (TEDs) $\tilde{R}(t_s,t_i)$ as

$$\tilde{R}(t_s,t_i)=\langle\hat{n}_t(t_s)n_t(t_i)\rangle=\mathrm{Tr}[\hat{a}_t^\dagger(t_s)\hat{a}_t^\dagger(t_i)\hat{a}_t(t_i)\hat{a}_t(t_s)\hat{\rho}]$$

$$=\int d\omega_p \mathcal{A}_p(\omega_p)\int d\Omega |f(\Omega;\omega_p)|^2 e^{-i(t_s-t_i)\Omega}$$

$$=\int d\Omega\int d\omega_p \mathcal{A}_p(\omega_p)|f(\Omega;\omega_p)|^2 e^{-i(t_s-t_i)\Omega}$$

$$=\int d\Omega R_i(\Omega)e^{-i(t_s-t_i)\Omega}. \quad (33)$$

Note that in the third line, we have interchanged the order of integration, leading to a Fourier transform relationship between the SI and the TED (fourth line).

3. SPECIFIC EXAMPLE: ILLUSTRATION OF THE SPECTRAL/TEMPORAL PHOTON-PAIR PROPERTIES

With the help of the above theory, we can now describe the spectral and temporal properties of the two-photon state produced by SFWM in a specific source design. In this section we present simulations of the photon-pair properties of interest, assuming experimental parameters consistent with our experiments described in Section 4. Let us consider a fused silica sphere of radius $R=135$ μm. For this radius, the degenerate SFWM frequency $\omega_s=\omega_i=\omega_p=2\pi c/1550.92$ nm corresponds most closely with azimuthal index values $l_s=l_i=774$ [i.e., this value of l comes closest to fulfilling the resonance condition $k(\omega_l)L=2\pi l$].

In Figs. 2(a) and 2(b) we plot for two values of the Q parameter (namely $Q=10^6$ and $Q=10^8$), for a radius of 135 μm, the phasematching strength $|g_{\vec{l}_p\vec{l}_s\vec{l}_i}(\omega_p,\Omega)|^2$, as a function of the pump frequency ω_p in the horizontal axis and the signal-photon generation frequency (detuned from the pump) Ω in the vertical axis. Note that fixing the input pump power to $P_{\mathrm{in}}=7$ mW, the Q value defines $2\gamma P$ through Eq. (14). In each of the plots we also show the phasematching contours $L\Delta k=0$ and $L\Delta k=0.49$, the latter value chosen because it yields $\mathrm{sinc}(L\Delta k/2)\approx 0.99$. In addition, a rectangle appearing close to the center of each plot represents the pump/generation spectral region of interest in our experiments. From these plots we can draw the following two conclusions: (i) the phasematching term $g_{\vec{l}_p\vec{l}_s\vec{l}_i}(\omega_p,\Omega)$ is essentially constant within the spectral area of interest; (ii) changes in the nonlinear term $2\gamma P$ (within the experimental range of interest) do not affect the resulting photon-pair properties. What this means is that we are able to approximate $g_{\vec{l}_p\vec{l}_s\vec{l}_i}(\omega_p,\Omega)\approx 1$, with the implication that the two-photon state will be entirely determined by the cavity properties through the Airy functions $\mathcal{A}_p(\omega)$, $\mathcal{A}_s(\omega)$, and $\mathcal{A}_i(\omega)$, as in the second line of Eq. (31).

In this context, so as to illustrate the effect of using extended rather than micro-cavities, in Figs. 2(c) and 2(d) we show, for cavity radii of 1.35 cm and 1.35 m and a Q value of $Q=10^8$ the phasematching strength $|g_{\vec{l}_p\vec{l}_s\vec{l}_i}(\omega_p,\Omega)|^2$, as a function of ω_p and Ω. As in panels Figs. 2(a) and 2(b) we show with a rectangle the spectral area of interest in our experiments. Note that in contrast with microcavities which are the focus of this work, for extended cavities phasematching does become a relevant factor in defining the two-photon state.

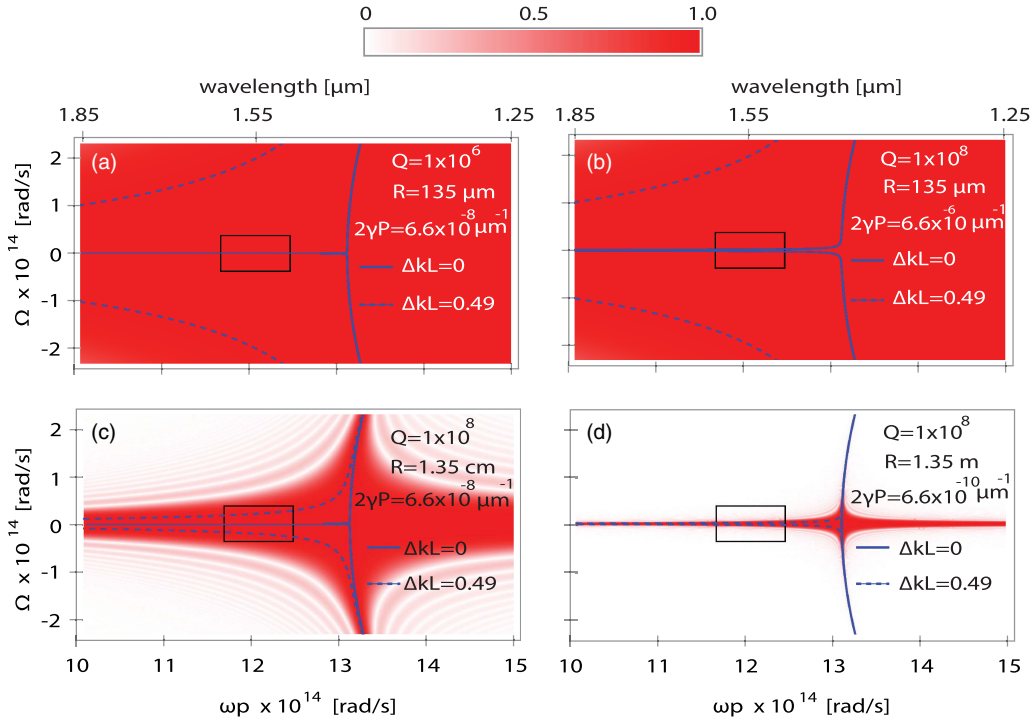

Fig. 2. (a) and (b) Density plots of the phase-matching function $|\mathrm{sinc}(L\Delta\kappa_{\bar{l}_p\bar{l}_s\bar{l}_i}(\omega_p,\Omega)/2)|^2$; also shown are the specific contours defined by $L\Delta k = 0$ and $L\Delta k = 0.49$ [which correspond to $\mathrm{sinc}(L\Delta k/2)$ equal to 1 and 0.99, respectively], for a sphere with $R = 135$ μm, for two values of Q, as indicated. The black rectangle indicates the region of interest in our experiments, centered around 1550 nm. (c) and (d) Plots similar to (a) and (b), for $Q = 10^8$ and much larger radii ($R = 1.35$ cm and $R = 1.35$ m).

Considering the discussion above, it is the cavity resonances for the signal and idler modes, as well as for the pump, that determine the two-photon state. Note that along the signal frequency ω_s axis, the two-photon amplitude can be non-zero only within each of the resonances (each corresponding to a particular value of l_s), and likewise for the idler frequency ω_i axis. Therefore, the two-photon state can be non-zero in $\{\omega_s, \omega_i\}$ space only within each particular mode belonging to a matrix of modes, defined by all combinations of l_s and l_i, centered around $l_s = l_i = 774$.

We point out that the spectral separation between two neighboring spectral modes, also known as FSR, has a slight dependence on frequency, as plotted in Fig. 3(a) from Eq. (4). The effect of such a spectral drift in the FSR on the two-photon state structure is illustrated in Figs. 3(b)–3(e). In Fig. 3(b) we present an illustration in $\{\omega_s, \omega_i\}$ space of the matrix of generation modes under the assumption of a constant FSR. We also indicate in this plot the rotated axes ω_+ and Ω, where a particular monochromatic pump corresponds to fixing the value of ω_+ as $\omega_+ = \omega_p$. An appropriate choice of ω_p so as to ensure overlap with the vertices of the resulting squares leads to a state in the form of a frequency comb along the main diagonal of the generation-mode matrix, as indicated in the figure. In Fig. 3(c) we show the same information in a rotated frequency space $\{\omega_+, \Omega\}$, so that the generation modes appear along a horizontal line. Figures 3(d) and 3(e) are analogous to Figs. 3(b) and 3(c), except that we have included the effect of the spectral drift of the FSR. It can be appreciated that

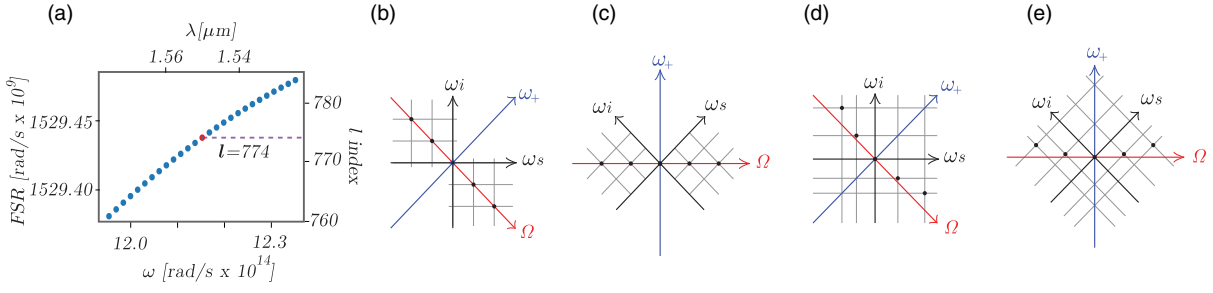

Fig. 3. (a) FSR versus optical frequency, calculated from Eq. (4); (b) and (c) sketch of generation-mode matrix assuming a constant FSR, plotted versus ω_s and ω_i [in panel (b)], and versus Ω and ω_+ [in panel (c)]; (d) and (e) sketch of generation-mode matrix assuming an FSR with spectral drift, plotted versus ω_s and ω_i [in panel (d)], and versus Ω and ω_+ [in panel (e)].

the two-photon state structure now increasingly departs from the diagonal for large $|\Omega|$ (with a concave locus of all possible generation modes).

In our two-photon state modeling, a prominent role is played by the resonance function for the pump $\mathcal{A}_p(\omega)$. This function may be characterized experimentally; see Section 4.A. While in Fig. 3 we present sketches designed to explain the geometry of the resulting SFWM two-photon state, in Fig. 4 we present an actual plot of the joint spectral intensity (SI) $|f_2(\omega_s, \omega_i; \omega_p)|^2$ [see Eq. (25)] for the specific case of a sphere of $R = 135$ μm radius, assuming Q values for the signal and idler modes of $Q_s = Q_i = 1 \times 10^8$, and a full width at half-maximum width for function $\mathcal{A}_p(\omega)$ of 20.4 MHz. Note that we have plotted the joint SI at each location on the main diagonal of the generation-mode matrix, within a square of 300 MHz side, and a center-to-center square separation of 1.52 THz. In this plot, we have included along each of the ω_s, ω_i, and Ω (diagonal) axes the resulting marginal intensity distributions. In the inset, we show the central square corresponding to $l_s = l_i = 774$, where we also include plots of $\mathcal{A}_s(\omega)$, $\mathcal{A}_i(\omega)$, and $\mathcal{A}_p(\omega)$, along each of the ω_s, ω_i, and ω_+ axes.

In order to further clarify the two-photon state structure, we plot in Fig. 5 within similar square regions as in Fig. 4 (this time defined in the rotated variables $\{\Omega, \omega_+\}$), the function $\mathcal{A}_s(\omega_+ + \Omega)$ in Fig. 5(a), the function $\mathcal{A}_i(\omega_+ - \Omega)$ in Fig. 5(b), the product $\mathcal{A}_s(\omega_+ + \Omega)\mathcal{A}_i(\omega_+ - \Omega)$ in Fig. 5(c), and the product $\mathcal{A}_s(\omega_+ + \Omega)\mathcal{A}_i(\omega_+ - \Omega)\mathcal{A}_p(\omega_+)$ in Fig. 5(d). Here, we may appreciate the effect already discussed through the sketches in Fig. 3, in which the generation modes increasingly depart from the axis $\omega_+ = \omega_p$ for larger values of $|\Omega|$. In Fig. 5(c), we also indicate with two dotted lines the width of the pump resonance function $\mathcal{A}_p(\omega_+)$. The result is that the generation modes lie increasingly outside of the pump resonance and are therefore suppressed for large $|\Omega|$, as is clear in Fig. 5(d). In Fig. 5(e), we show the resulting photon pair SI in the form of a frequency comb, as is obtained from Eq. (31).

In Fig. 6, we show the idler–photon SI, similar to that shown in Fig. 5(e), for three different signal/idler Q values (1×10^6, 1×10^7, and 1×10^8), where we also indicate the corresponding cavity reflectivity coefficients. Note that for a comparatively smaller Q parameter, resulting in spectrally broader generation modes, the envelope decays more slowly because spectral overlap is retained with the pump resonance function $\mathcal{A}_p(\omega)$ over a larger span of Ω values.

It is of interest to provide a temporal description of the two-photon state in addition to the spectral description already provided. In Fig. 7 we show, as calculated numerically from Eq. (33) and from the traces in Fig. 6, the TED for the same three Q values [Figs. 7(a)–7(c)]. Note that each of these three

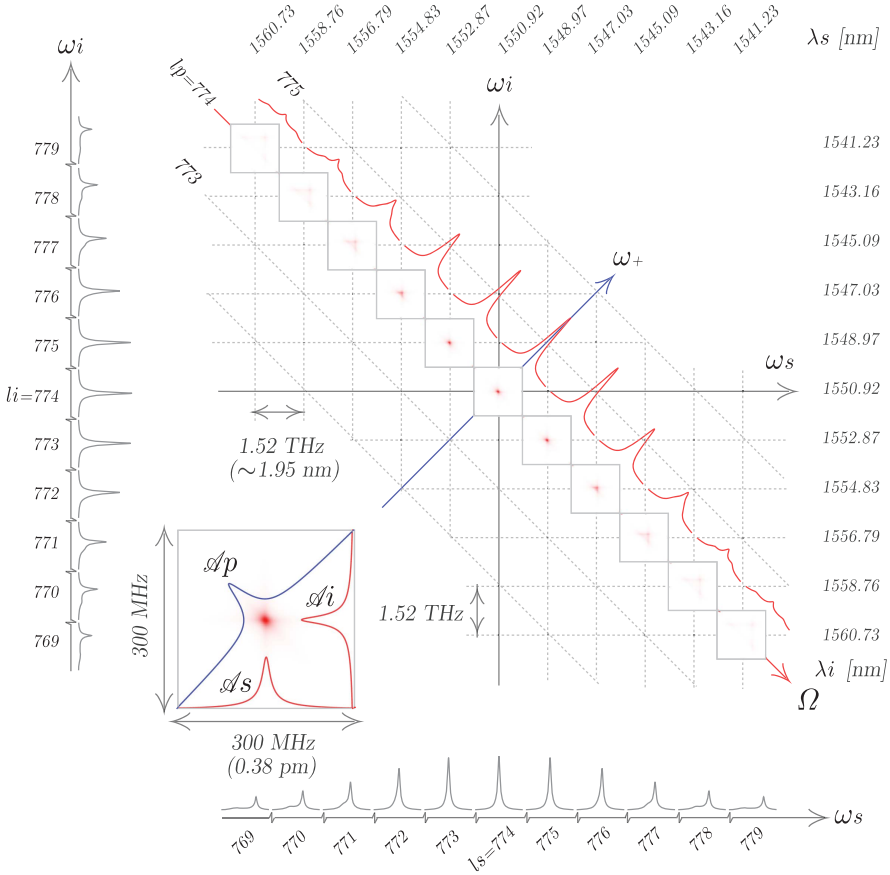

Fig. 4. For a microsphere with radius $R = 135$ μm and $Q_s = Q_i = 1 \times 10^8$, two-dimensional plot of the joint SI [computed from Eq. (25)], plotted within a region of 300 MHz width, centered at each point of the generation mode-matrix main diagonal (with a separation of 1.52 THz between regions along $\omega_{s,i}$); inset, close-up of central region, corresponding to $l_s = l_i = 774$.

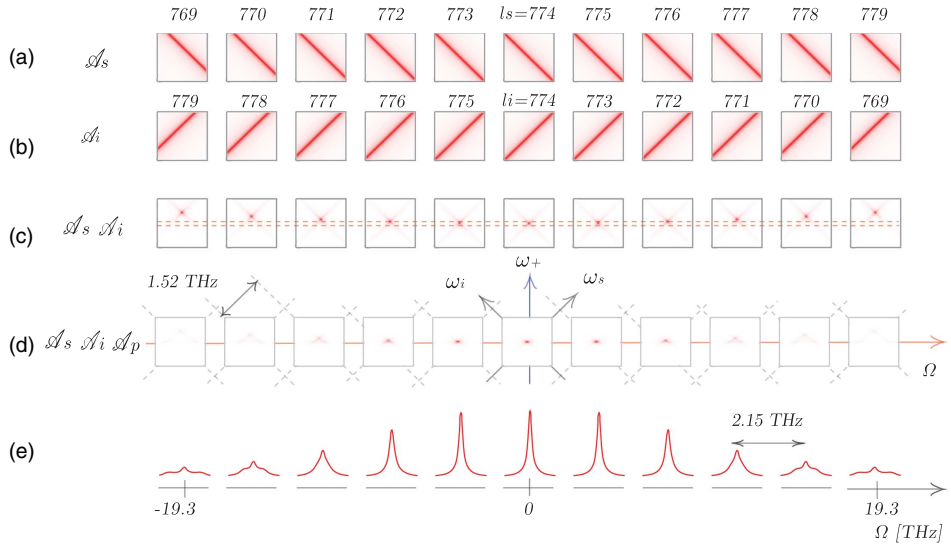

Fig. 5. This figure clarifies the structure of the two-photon state produced by SFWM in a microsphere device, in regions similar to those defined in Fig. 4 for the same source, in the frequency variables Ω and ω_+. We show plots of the function $\mathcal{A}_s(\omega_+ + \Omega)$, $\mathcal{A}_i(\omega_+ - \Omega)$, $\mathcal{A}_s(\omega_+ + \Omega)\mathcal{A}_i(\omega_+ - \Omega)$, and $\mathcal{A}_s(\omega_+ + \Omega)\mathcal{A}_i(\omega_+ - \Omega)\mathcal{A}_p(\omega_+)$ in each of rows (a) through (d). Note that in (c) we have indicated with a pair of dotted lines the spectral width of the pump resonance. In (e), we show a plot of the function $R_i(\Omega)$, obtained by integrating $\mathcal{A}_s(\omega_+ + \Omega)\mathcal{A}_i(\omega_+ - \Omega)\mathcal{A}_p(\omega_+)$ over ω_+ [or equivalently over ω_p; see Eq. (31)], yielding the idler-photon SI in the form of a frequency comb.

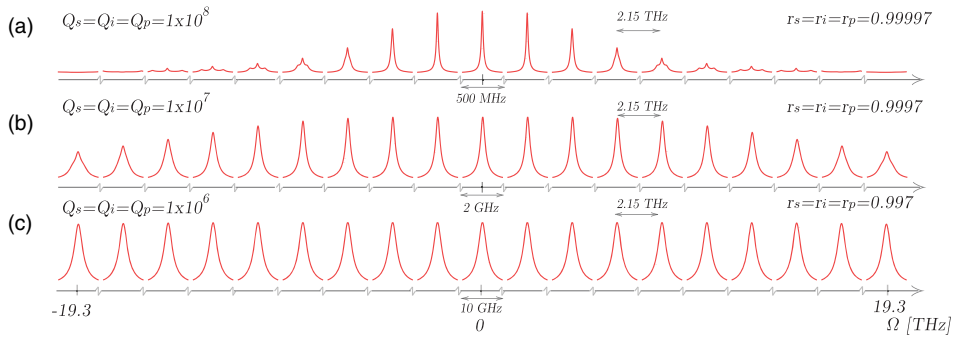

Fig. 6. In this figure, we show the behavior of the idler-photon SI $R_i(\Omega)$, for the same source as assumed in the previous two figures [computed from Eq. (31); see also Fig. 5], for three different values of the Q coefficients [$Q = 10^8$ in (a), $Q = 10^7$ in (b), and $Q = 10^6$ in (c)], assumed to be the same for both signal and idler modes.

functions exhibits an envelope with closely spaced oscillations (with a period corresponding to the cavity round-trip time), which cannot be resolved in those plots. In Fig. 7(d), we show a closeup of the curve shown in Fig. 7(a), within the region of the maximum showing these temporal oscillations.

As can be appreciated from Fig. 6, the resulting single-photon SI is in the form of a frequency comb, with the relative heights of the peaks modulated by an envelope function. While the FSR exhibits a slow frequency dependence [as indeed has been shown in Fig. 6(a)], within a restricted spectral window

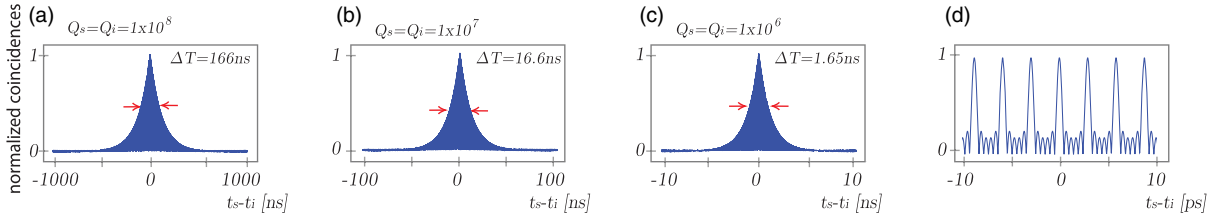

Fig. 7. In panels (a)–(c) of this figure, we show plots of the TED function $\tilde{R}(T)$ (with $T = t_s - t_i$), obtained for the same source as assumed for Figs. 6(a)–6(c), for three different values of $Q = Q_s = Q_i$. (d) Close-up around the central region of the plot in (a), showing the temporal oscillations with period equal to the cavity round-trip time, which cannot be resolved in panels (a)–(c).

we may model the SI function as a fixed FSR comb function as follows:

$$R_i(\Omega) = H(\Omega) \cdot h(\Omega) * \mathrm{comb}_{\delta\Omega}(\Omega), \tag{34}$$

where $H(\Omega)$ represents the envelope function, $h(\Omega)$ represents an individual peak in the comb, and the symbol $*$ denotes a convolution. In addition, this equation is written in terms of the Dirac–delta comb function $\mathrm{comb}_{\Delta}(x)$, defined as follows:

$$\mathrm{comb}_{\Delta}(x) = \sum_{j=-\infty}^{\infty} \delta(x - j\Delta). \tag{35}$$

Let functions $\tilde{H}(T)$ and $\tilde{h}(T)$ represent the Fourier transforms of $H(\omega)$ and $h(\omega)$, respectively. Under the assumption that the function $\tilde{H}(T)$ is much narrower than function $\tilde{h}(T)$, we can then write the joint temporal intensity (or temporal emission distribution, TED, function) $\tilde{R}(T)$, with $T = t_s - t_i$, as follows:

$$\tilde{R}(T) = \tilde{h}(T) \cdot \tilde{H}(T) * \mathrm{comb}_{1/\delta\Omega}(T). \tag{36}$$

Thus, the joint temporal amplitude function is composed of a comb function in the temporal variable $T = t_s - t_i$ with individual comb peaks defined by the function $\tilde{H}(T)$, with a peak-to-peak separation of $1/\delta\Omega$, and an envelope function $\tilde{h}(T)$ that describes the roll-off in amplitude for large $|T|$. Interestingly, the roles of the function $H(\Omega)$ and $h(\Omega)$ in the frequency domain and $\tilde{H}(T)$ and $\tilde{h}(T)$ in the temporal domain are reversed. Specifically, the spectral envelope defines the functional dependence of each individual temporal comb peak, and the functional dependence of each individual frequency comb peak defines the envelope of the resulting comb in the temporal domain.

Note also that if a spectral filter is applied in such a manner that a single spectral peak $R_i(\omega) = h(\omega)$ survives, we may obtain the functional dependence of $h(\omega)$ from a numerical Fourier transform of the envelope of the TED $\tilde{h}(T)$. This will be relevant in our experiment, below, in which, while we lack the spectral resolution to resolve one comb peak, $h(\omega)$, we can nevertheless obtain this function $h(\omega)$ from a measurement in the temporal domain.

Note that it is possible to apply the converse of this idea: from an experimental measurement of the spectral envelope $H(\Omega)$ we could infer through a Fourier transform the functional form of a single temporal peak $\tilde{h}(T)$. We have not exploited this in our paper because the width of a single temporal peak is of less interest as compared to the width of a single-frequency comb peak, and because experimentally we do not obtain $H(\Omega)$ over the complete spectral range of interest, but only within the signal and idler spectral windows [see, for example, Fig. 10(b) below].

4. EXPERIMENT

In order to demonstrate the generation of submegahertz spectral bandwidth photon pairs through the SFMW process, fused silica microspheres are used. The microspheres are fabricated from SMF-28 fiber using a fusion splicer (Fujikura FSM100P). The 135–250 μm radius spheres remain supported by an optical fiber stem, facilitating placement and alignment in our experimental setup.

The experimental setup used for our main results (Fig. 12, as well as Fig. 13) is shown in Fig. 8. Note that a number of setup variations, as indicated in the figures below, are used to obtain the various measurements reported, leading to our main results.

We have used as a pump for the SFWM process a fiber-coupled, continuous-wave laser, tunable within the wavelength range 1550–1630 nm, with a linewidth of <200 kHz (New Focus TLB-6700). While the nominal linewidth is small, the laser can emit at a range of parasite frequencies. To remove extraneous modes, we have devised a filtering strategy involving a wavelength division multiplexing (WDM) device, followed by an erbium-doped fiber amplifier, followed by a second WDM device. We use two WDM devices, which we refer to as dense WDM (DWDM) on account of the comparatively small bandwidth of each channel, with a 0.57 nm measured full width at half-maximum (FWHM), as well as the comparatively small separation between channels (0.8 nm), spanning wavelengths from 1529.55 to 1560.61 nm. With the amplifier operating at a gain of 24 dB, the maximum usable laser power is 40 mW; typically, the present experiments used less than 7 mW.

In order to couple the laser beam from the DWDM device into the microsphere, an evanescent fiber taper waveguide coupler is used. An inline optical polarization controller is used to adjust the polarization in the optical fiber before coupling into the cavity.

A. Cavity Resonance Characterization: Setting up the SFWM Pump

In order to use our taper-sphere assembly, a first necessary step is to locate, and characterize, an appropriate resonance near 1550 nm, which may act as the pump for the SFWM process. For this purpose, the laser is continuously rastered across a range of wavelengths while we monitor the optical power emanating from the fiber taper output. The scan speed and time are optimized to eliminate any thermal effects that might distort the resonant line shape. In particular, we vary the laser frequency according to a triangular waveform with a 100 Hz frequency and a 25 GHz oscillation spread, while monitoring the transmitted power as recorded by a fast photodiode (Thorlabs Model DET10D), with its electronic output leading to a 2 GHz digital oscilloscope. An example of a measurement obtained in this way is shown in Fig. 9, where we plot the reduction in transmittance (transmittance at each frequency subtracted from the transmittance far from resonance) versus frequency. In addition to the experimental data, we also plot a best fit to an Airy function $\mathcal{A}_p(\omega)$, which exhibits an FWHM bandwidth of 20.4 MHz. Note that multiple measurements over several resonances and a number of devices (with different radii) lead to an approximate variation in the resonance bandwidth of ∼10%.

Once we have completed this step, we ensure that laser light can couple into the microsphere to act as the pump in the SFWM process. Note that thermal effects originating from the laser power confined in the microsphere result in a slight variation of the optical phase $k(\omega)L$ over time, which is a sufficiently large effect to bring the microsphere out of resonance with the incoming laser frequency. So as to circumvent this complication, we operate our experiments with the triangular

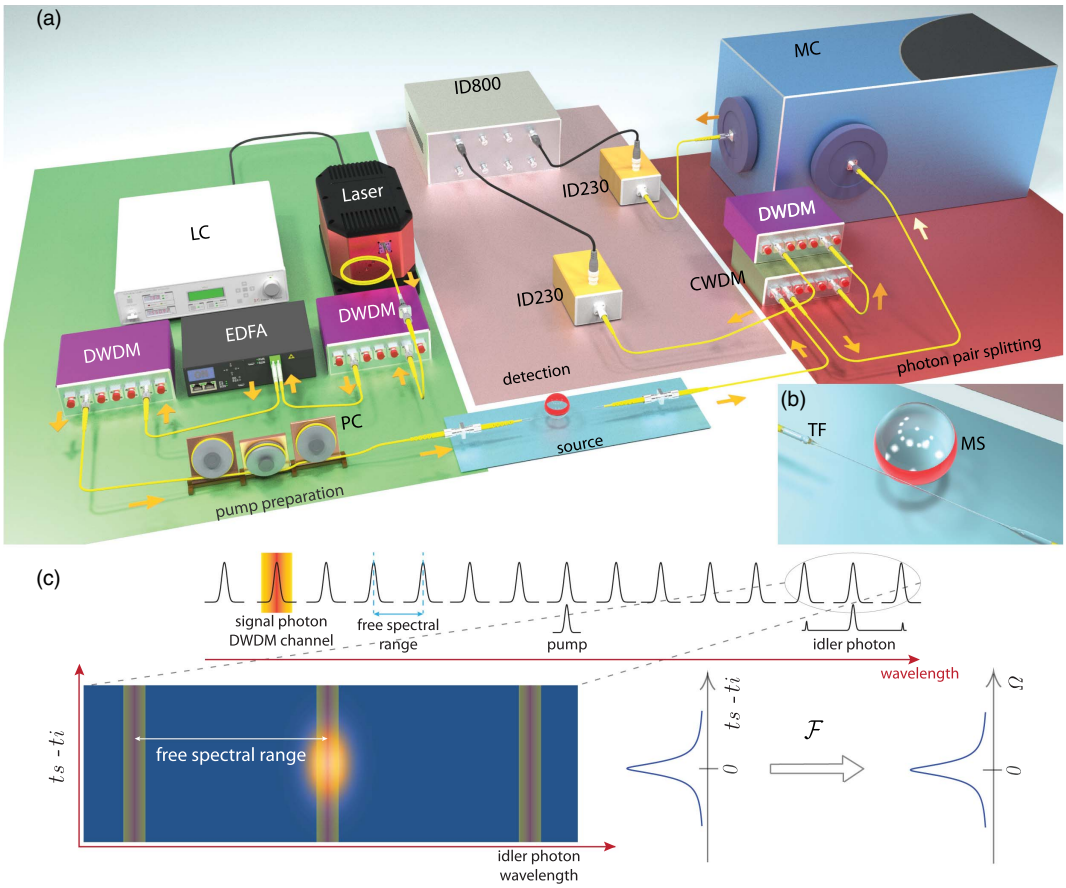

Fig. 8. (a) Experimental setup. LC, laser controller; DWDM, dense wavelength division multiplexing device; EDFA, erbium-doped fiber amplifier; PC, polarization controller; TF, tapered fiber; MS, microsphere; CWDM, coarse wavelength division multiplexing device; MC, grating-based monochromator; ID230, free-running InGaAs APD; ID800, time-to-digital converter. Note that in some of the subsequent figures we have provided a setup sketch to show variations on the setup shown in this figure. (b) Close-up showing the fiber taper-microsphere system; (c) schematic of source operation and data obtained in our measurements.

variation of the laser frequency described above, thus ensuring that even if the system is brought out of resonance, it periodically returns to being on resonance at two points of each oscillating period. Note that the oscillation spread (25 GHz) is much greater than the width of the resonance (see Fig. 9), which in turn is much greater than the pump linewidth.

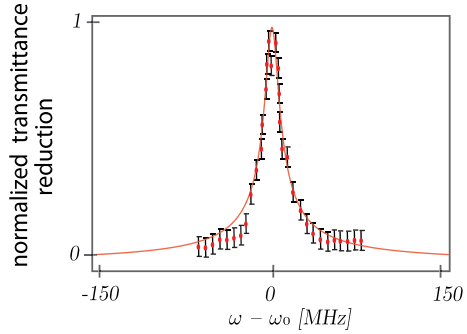

Fig. 9. Experimentally obtained normalized transmittance reduction versus ω (calculated as the difference between transmission far from the resonance and the transmittance at each ω), for a particular cavity resonance, shown together with an Airy function $\mathcal{A}_p(\omega)$ fit.

We point out that our SFWM theory presented in Section 2 accounts for this pump frequency variation by modeling the two-photon state as a statistical mixture of the pure states produced by each individual frequency within the pump resonance, as defined by function $\mathcal{A}_p(\omega)$.

B. Single-Photon Frequency Comb Characterization

While operating on-resonance, the microsphere presents a spectral comb of resonances. Note that the three waves involved in the SFWM process (degenerate pump, signal, and idler) must exhibit frequencies ω_p, ω_s, and ω_i, matching one or more of these cavity resonances. For a given combination of pump and signal-photon frequencies ω_p and ω_s, the idler photon will appear at a frequency $\omega_i = 2\omega_p - \omega_s$, as mandated by energy conservation.

In order to demonstrate the emission of SFWM photon pairs, we use the fact that the three waves involved (pump, signal, and idler) are all at different optical frequencies. Thus, the output signal from the tapered fiber is sent to a coarse wavelength division multiplexing (CWDM) device, which can send each of the three waves to a different output channel, as shown in the setup sketch in Fig. 10(a). This CWDM device has transmission windows with an FWHM-measured width of

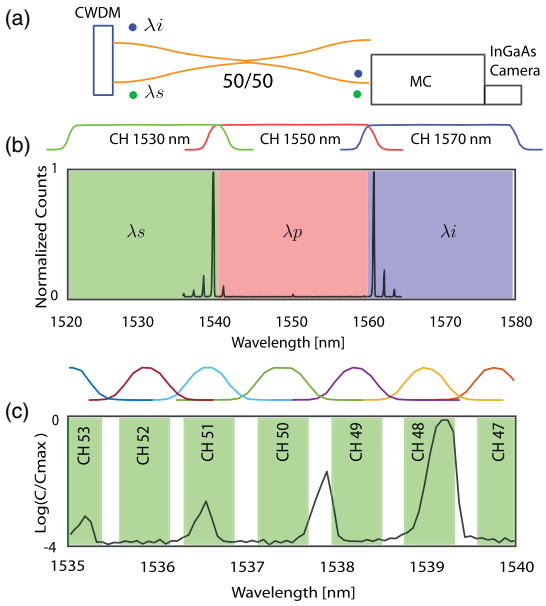

Fig. 10. (a) Sketch of the experimental setup used for the characterization of the signal-idler SFWM spectrum; (b) SFWM spectrum, composed of pairs of energy-conserving peaks, also showing regions colored red, green, and blue, indicating each of three relevant CWDM channels. We have included the measured transmission curves for these three CWDM channels. (c) For the signal photon, i.e., corresponding to $\lambda < \lambda_p$, the individual emission peaks (shown using a logarithmic scale), along with a map of the DWDM channels used, including the transmission curves for each of these channels.

22 nm, separated by 20 nm (i.e., neighboring channels overlap), ranging from 1270 to 1610 nm. Note that there are three outgoing CWDM channels that are of interest, centered at 1530, 1550, and 1570 nm, as indicated with the colors green, red, and blue, in Fig. 10(b), where we have also shown the experimentally obtained channel transmission curves. Note that while the pump lies in the 1550 nm channel, the signal-photon band lies mostly in the 1530 nm channel (red) and the idler-photon band lies mostly in the 1570 nm channel (blue).

We connect a single-mode fiber to each of the 1530 and 1570 nm channel outputs, thus splitting the SFWM pairs into two distinct spatial modes, each traveling in a distinct fiber. In order to visualize all SFWM generation peaks in a single spectral measurement, we first connect the two CWDM outputs into the two input ports of a 50:50 fiber beam splitter, with one of the outputs leading to a grating spectrometer, with an InGaAs detection array (Andor Idus CCD camera) used as sensor; the experimental setup is sketched in Fig. 10(a). The photon pairs are generated with the signal band roughly at 1540 nm and the idler band roughly at 1560 nm. The result is the black curve in Fig. 10(b) showing three pairs of energy conserving peaks, along with two additional smaller peaks on the low-wavelength channel without an evident counterpart in the large-wavelength channel.

It becomes clear from the frequency comb obtained for each of the signal and idler photons [see Fig. 10(b)] that there is one dominant pair of peaks (in terms of peak height). With the purpose of spectrally isolating this dominant pair of peaks, we filter the signal photon with a DWDM channel. In Fig. 10(c) we show the same four peaks on the $\lambda < \lambda_p$ side, which are transmitted by the 1530 nm CWDM channel (plotted in a logarithmic scale), together with the available DWDM spectral windows. Thus, by transmitting the signal photon through DWDM channel 48, we can indeed isolate the tallest signal-photon peak. In the next subsection, we perform an analysis of the coincidence count rate between the signal photon transmitted through the 1530 nm CWDM channel and through DWDM channel 48, with the idler photon transmitted through the 1570 nm CWDM channel.

C. Initial Coincidence Count Rate Analysis

The pairs of peaks described in the previous subsection are energy-conserving, which suggests that they are produced by an SFWM process. However, the photon pair nature of the emitted light can be confirmed through a coincidence-counting measurement between the signal and idler photons. For this purpose, as has already been mentioned, we isolate the tallest pair of peaks shown in Fig. 11(a) by transmitting the signal photon ($\lambda < \lambda_p$) through channel 48 of a DWDM (identical

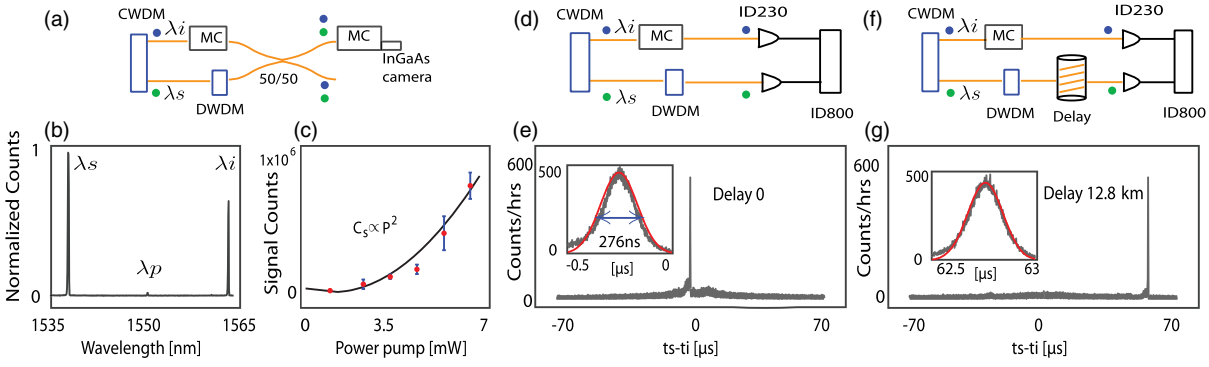

Fig. 11. (a) Sketch of the setup used for the results shown in (b) and (c); (b) isolation of tallest pair of energy-conserving peaks from Fig. 10(a), obtained by filtering the signal photon with a DWDM channel and the idler photon with a grating monochromator; (c) total SFWM flux, integrated within the signal-mode peak in (b), as a function of pump power, along with a quadratic fit; (d) sketch of the setup used for the results shown in (e); (e) coincidence count rate as a function of the detection time difference between the signal and idler modes, presenting a well-defined peak near zero delay; inset, peak close-up; (f) sketch of the setup used for the results shown in (g); (g) similar to panel (e), but the signal photon is transmitted through a 12.8 km stretch of fiber.

to the ones described above for filtering the pump). In addition, we transmit the idler photon ($\lambda > \lambda_p$) through a grating monochromator, with its transmission window centered at the energy-conserving idler-mode frequency $2\omega_p - \omega_s$.

In order to verify the energy conservation in this isolated pair of peaks, the DWDM-filtered signal photon (channel 48) is combined with the monochromator-filtered idler photon at a 50:50 fiber beam splitter, and one of the outputs is sent to a second monochromator with its output leading to an InGaAs detection array (Andor Idus one-dimensional CCD camera); the setup used is shown in Fig. 11(a). The result of this measurement is presented in Fig. 11(b), clearly showing a single pair of energy-conserving peaks. At this point, we also performed SFWM counts versus pump power measurement by numerically integrating the counts contained in the signal ($\lambda < \lambda_p$) photon as a function of the pump power. The results are shown in Fig. 11(c) along with a quadratic best fit, indicating that the emitted power indeed has a quadratic dependence on the pump power, as is expected for the SFWM process [13].

In order to experimentally observe coincidence events between the spectrally filtered photons in each pair, we use the setup sketched in Fig. 11(d), connecting the two fibers carrying the signal and idler generation modes to the entrance ports of two free-running InGaAs avalanche photodiodes (APDs; IDQuantique 230). The electronic pulses produced by the APDs are sent to a time-to-digital converter (IDQuantique ID800) so as to monitor the distribution of signal-idler time detection differences. The results show a very well-defined peak near zero signal-idler delay [Fig. 11(e)]. This peak corresponds to the detection of the idler photon, conditioned by the detection of the corresponding signal photon transmitted through the selected DWDM channel. This peak has an FWHM of 276 ns and shows a temporal shift of 278 ns, which we believe is due to an imbalance in the Q factor of the microsphere for the signal and idler photons. In other words, the cavity lifetime for the signal photon is longer than that of the idler photon by a time duration roughly corresponding to the width of the TED. As an additional test, we performed a related experiment in which we transmit the signal photon over a 12.8 km length of optical fiber, acting as a delay line, before reaching the corresponding APD [Fig. 11(f)]. The resulting distribution of time of emission differences is presented in Fig. 11(g) and shows a temporal shift (62.7 μs) corresponding to the delay due to the 12.8 km length of optical fiber.

As we have seen, DWDM channel 48, acting on the signal photon, can transmit the tallest signal-frequency comb peak while suppressing all other peaks. Thus, when monitoring *coincidence* events as a function of the idler frequency (with the help of a grating-based monochromator), likewise, only the tallest idler peak survives. However, the minimum frequency step $\delta\omega_{\mathrm{MC}} \approx 39$ GHz that can be resolved by the monochromator is orders of magnitude larger than the spectral width of the single photons (in the region of megahertz), determined by the large Q values of our resonator. This means that while the monochromator is useful in order to spectrally situate the idler photon to within $\delta\omega_{\mathrm{MC}}$, we are in fact unable to resolve the functional dependence of an individual frequency comb peak. In the next subsection, we will discuss a strategy based on temporally resolved detection to overcome this limitation.

D. Time-Resolved and Frequency-Constrained Coincidence Count Rate Analysis

As we have already discussed, in the context of Figs. 11(e) and 11(g), we are able to measure the TED envelope [corresponding to $\tilde{h}(T)$; see Eq. (36)], with characteristic times in the hundreds of nanoseconds.

As discussed at the end of Section 3, under the assumption that a single peak in the frequency comb can be isolated (although not resolved), we may recover the functional dependence of a single idler-photon comb peak, i.e., $h(\Omega)$, through the Fourier transform of the function $\tilde{h}(T)$ obtained experimentally. In Fig. 8(c), we present a schematic of the overall operation of our experiment: each of the pump, signal, and idler modes appears at one of the cavity resonances (i.e., are aligned with one of the cavity frequency comb peaks); the detection of a signal photon with frequency ω_s, transmitted through a DWDM channel, heralds an idler photon, which is detected following passage through the monochromator set to transmit a frequency $\omega_i = 2\omega_p - \omega_s$ (thus, while sweeping ω_i, a peak appears at the energy-conserving value); the one-dimensional TED envelope $\tilde{h}(T)$ obtained for a fixed idler transmission center frequency is Fourier-transformed to yield the functional dependence of one idler-photon comb peak $h(\Omega)$.

Following the strategy explained above, we carry out a measurement in which we spectrally filter the signal photon (with a DWDM channel) as well as the idler photon (i.e., we constrain it to the spectral transmission window of the monochromator) and, in addition, we temporally resolve each coincidence event while sweeping ω_i. Specifically, we measure the signal-conditioned idler TED as a function of the idler center frequency transmitted through the monochromator. We thus obtain a two-dimensional density plot with the time of emission difference T in the vertical axis and the idler wavelength λ_i in the horizontal axis. This type of measurement, carried out with the full setup shown in Fig. 8, leads to our main experimental results, presented below.

The emission characteristics are dependent mainly on two experimental variables: the microsphere radius and the pump frequency. To investigate this dependence, we have conducted a systematic experimental study for distinct radius–pump wavelength combinations.

First, for a microsphere with $R = 180$ μm, the pump transmitted through DWDM channel 33 ($\lambda = 1550.92 \pm 0.25$ nm), and the signal photon transmitted through channel 47 ($\lambda = 1539.77 \pm 0.25$ nm), Fig. 12(a) shows the resulting two-dimensional spectrogram. For the SFWM process, the observation of conditioned idler photons is expected at the energy-conserving frequency. In our measurement, we indeed observe a very well-defined peak centered at the energy-conserving frequency, with residual accidental events appearing at multiples of the FSR (FSR = 1.4 nm). Note that since we are not able to spectrally resolve the peaks, their apparent width is determined by the effective spectral resolution in our setup, around 0.5 nm. In Fig. 12(b), we show a marginal spectral distribution obtained by numerically integrating over variable T within the interval denoted by the dotted white lines, and in Fig. 12(c), we

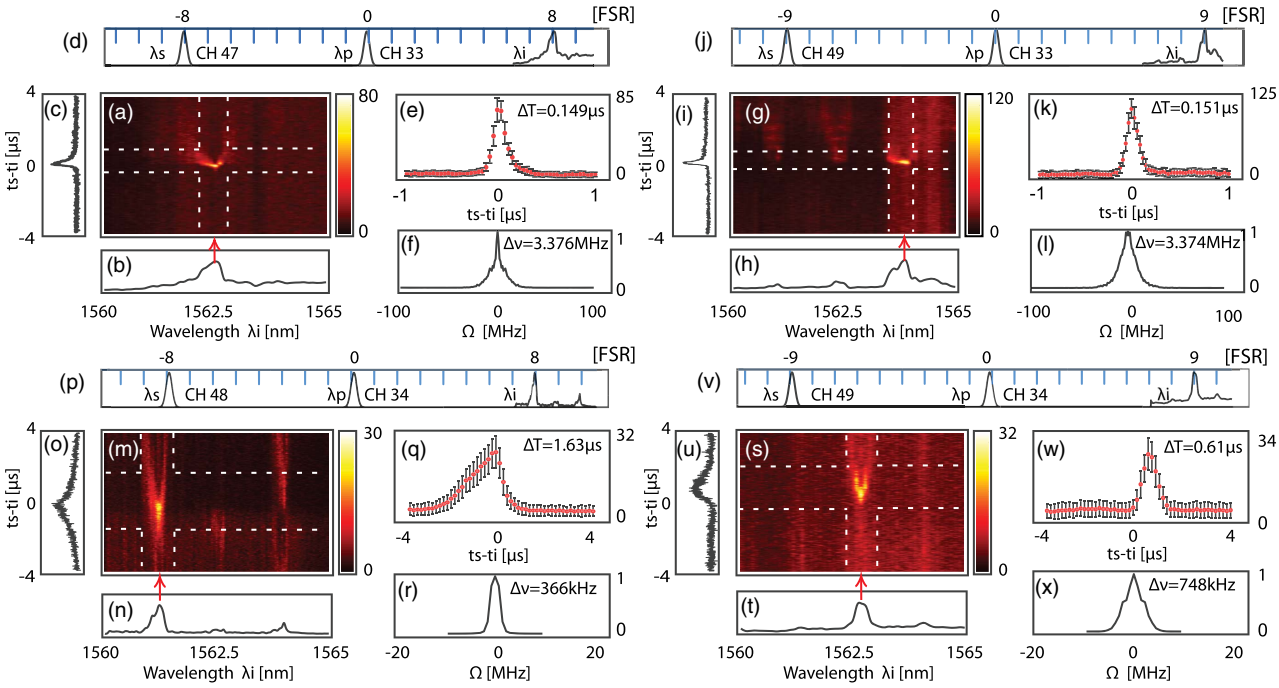

Fig. 12. For a microsphere with $R = 180$ μm, the pump transmitted through DWDM channel 33, and the signal photon transmitted through DWDM channel 47. (a) Heralded idler photon emission characteristics in the space formed by the idler wavelength λ_i and the signal-idler time of detection difference $T = t_s - t_i$; (b) marginal distribution in λ_i; (c) marginal distribution in variable T; (d) graphical representation of wavelengths involved for the pump, signal, and idler modes, for idler frequency denoted by red arrow in (a); (e) measured TED; (f) inferred idler-mode single-photon intensity spectral distribution. Panels (g)–(l) are similar to panels (a)–(f), except that DWDM channel 49 is used, instead of 47, to transmit the signal photon. For a microsphere with $R = 180$ μm, the pump is transmitted through DWDM channel 34, and the signal photon is transmitted through DWDM channel 48. (m) Heralded idler photon emission characteristics in the space formed by the idler wavelength λ_i and the signal-idler time of emission difference T; (n) marginal distribution in λ_i; (o) marginal distribution in variable T; (p) graphical representation of wavelengths involved for the pump, signal, and idler modes, for idler frequency denoted by red arrow in (m); (q) measured time of emission difference distribution; (r) inferred idler-mode single-photon intensity spectral distribution; panels (s)–(x) are similar to panels (m)–(r), except that DWDM channel 49 is used, instead of 48, to transmit the signal photon.

show a marginal distribution in the time of emission difference T obtained by numerically integrating over the frequency, again within the interval denoted by dotted white lines. The relevant pump and generation wavelengths are summarized in Fig. 12(d), which shows the DWDM transmission windows used for the pump and signal modes, as well as the resulting measured spectral width of the idler photon. In this figure, we also indicate the microsphere resonance wavelengths.

It is of interest to measure the TED envelope, corresponding to function $\tilde{h}(T)$ [see Eq. (36)], for a given filtering configuration, i.e., for a given choice of DWDM channel (signal photon) and a given monochromator spectral window (idler photon). Figure 12(e) shows the measured TED envelope for the signal photon transmitted through DWDM channel 47 and for the monochromator set to transmit the idler frequency $\omega_i = 1206.37$ THz, indicated with a red arrow in panel (a). Figure 12(f) shows the single-photon spectral profile $h(\Omega)$ of the heralded idler photon, obtained as explained in Section 3, from the Fourier transform of the TED, or $\tilde{H}(T)$. The observed bandwidth of the heralded idler photon (expressed in natural rather than angular frequency) of $\Delta\nu = 3.376$ MHz is remarkably small, corresponding to a remarkably large idler photon Q parameter (obtained as $\omega_i/\Delta\Omega$, where ω_i is the central idler frequency) of 0.57×10^8. Note that microspheres tend to exhibit a larger Q parameter as compared with other microresonator geometries (such as microrings [14,15,24,25,27–29,42] and microtoroids [43]), which implies on the one hand a smaller attainable photon pair bandwidth, and on the other hand, also implies that the SFWM photon pair emission rate for a given pump power level will be higher.

In the SFWM process with a narrowband pump, we expect strict spectral correlations between the signal and idler photons, as indeed is implied by Eq. (11). Therefore, shifting the signal photon filtering to a different wavelength (i.e., selecting a different DWDM channel), we expect a corresponding spectral shift for the idler photon as recorded by the monochromator-based measurement. The experimental verification of such spectral shifting due to signal-idler spectral correlations is presented in Figs. 12(g)–12(l). Concretely, shifting the signal DWDM channel from 47 to 49 (corresponding to a central channel wavelength shift from 1539.77 to 1538.19 nm), results in a shift in the idler photon that is apparent in Fig. 12(g), which is to be compared with Fig. 12(a). In the remaining panels, we have shown analogous plots to those in the left-hand side of the figure: marginal spectral distribution for the idler photon in Fig. 12(h); marginal time of emission difference

distribution for the idler photon in Fig. 12(i); summary of the spectral characteristics of the pump, signal, and idler modes in Fig. 12(j); TED for a given filtering configuration in Fig. 12(k); and single-photon spectral profile inferred for the heralded idler photon in Fig. 12(l). The resulting spectral width (3.374 MHz) and Q parameter (0.56×10^8) values are similar to the ones in the earlier configuration.

The second part of Fig. 12 contains a complementary set of data, for a different combination pump wavelength. In the first combination, the pump wavelength is changed to 1550.12 nm, transmitted by DWDM channel 34 instead of 33, while leaving the microsphere radius the same. The qualitative behavior is similar to the earlier presented findings when the pump was in DWDM channel 33, and the heralded idler photon exhibits a considerably smaller emission bandwidth (again expressed in terms of natural rather than angular frequency) of 366 and 748 kHz versus 3.376 and 3.374 MHz, and larger Q values, 5.3×10^8 and 2.5×10^8 versus 0.57×10^8 and 0.56×10^8, as compared to the results with the pump at DWDM channel 33 (Fig. 12). We note that this represents, to the best of our knowledge, the shortest bandwidth for a heralded single photon (366 kHz) demonstrated to date, based on the SFWM process.

Note that in each two-dimensional data set with axes $\{\lambda_i, T\}$, 10,000 experimental data points were recorded across the range of T values; we grouped these data points in sets of either 100 [in the case of Figs. 12(e) and 12(k)] or 200 points [in the case of Figs. 12(q) and 12(w)], which were averaged to yield the one-dimensional TED functions with 100 data points for Figs. 12(e) and 12(k) and with 50 data points for Figs. 12(q) and 12(w). Error bars in each of the TED plots indicate the standard deviation among the 100 or 50 data points.

As we have studied in Sections 2 and 3, the resulting frequency comb envelope, which is affected by the spectral drift in the FSR discussed in Section 3 [see Fig. 3(a)], depends on the overlap of the functions $\mathcal{A}_p(\omega)$, $\mathcal{A}_s(\omega)$, and $\mathcal{A}_s(\omega)$. We remark that the envelope width apparent in our experimental data shown in Fig. 12 is broadly consistent with the simulated one in Fig. 7, for the experimental values of Q obtained in our experiment.

Note that in addition to the smaller bandwidth, the emission characteristics in the $\{\lambda_i, T\}$ space include a pair of "tails" that extend toward positive T values, the origin of which is left for a future study. In order to also show the idler-photon spectral shifting in response to shifting the signal-photon DWDM channel, we have filtered the signal photon with DWDM channel 48 in the left-hand side of the figure and with channel 49 in the right-hand side. It is clear that the idler photon shifts in frequency in response to selecting a different signal-photon DWDM channel, as we would expect for strict signal-idler spectral correlations.

To investigate the dependence of the heralded idler photon on the type of signal photon filtering method used, two different filtering systems were applied: wideband and narrowband. A slightly smaller radius microsphere was used (135 μm), and the pump laser is adjusted to 1550.92 nm, transmitted through DWDM channel 33. For this experiment, we have used two signal-photon spectral filtering configurations: a narrowband configuration based on DWDM channel 48 (centered at 1538.98 nm with a 0.5 nm width), and a wideband configuration based on the CWDM channel only (centered at 1530 nm with a 20 nm width); see Fig. 13. Figures 13(a) and 13(d) show the heralded idler photon emission characteristics in the $\{\lambda_i, T\}$ space, under narrowband and wideband signal-photon filtering, respectively. For each of these panels, we have shown a marginal distribution for λ_i, obtained by integrating over T; see Figs. 13(b) and 13(e), as well as a marginal distribution for T, obtained by integrating over λ_i; see Fig. 13(c). Note, on the one hand, that while the narrowband case results in a sharp peak, both in idler frequency and in time of emission difference, on the other hand, the wideband case shows an essentially constant response along T and three emission regions along λ_i separated by the FSR, i.e., corresponding to thee microresonator spectral modes. It is consistent with the existence of signal-idler spectral correlations that a wider filtered spectral signal-photon span will map to a similarly wider idler-photon spectral generation range, as is observed experimentally. It is also noteworthy that the fact that the wideband case is not peaked in the time of emission difference variable T suggests that the photon pair character is lost, probably as a result of noise mechanisms.

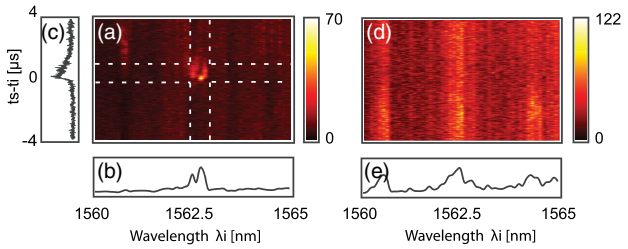

Fig. 13. For a microsphere with $R = 135$ μm, and the pump transmitted through DWDM channel 33, (a) and (d) show the idler mode, single-photon emission characteristics for narrowband filtering (DWDM channel 48) in (a), and for wideband filtering [1530 nm CWDM channel in (d)]. Panels (b) and (e) show spectral marginal distributions for the distributions in (a) and (d), respectively. Panel (c) shows a temporal marginal distribution for the distribution in (a).

Table 1 shows a summary of all experimental runs discussed above. For each specific experiment, we indicate the microsphere radius (in the first column); the central wavelength λ_s of the DWDM channel used to filter the signal photon, or CWDM in the case of the last run (in the second column); the idler wavelength $\lambda_i^{(0)}$ selected in order to display the TED (in the fourth column); the width of the temporal distribution (in the fifth column); the resulting heralded idler photon spectral width $\Delta\nu$ (in the sixth column); and the associated Q parameter (in the last column). The first four rows correspond to the data shown in Fig. 12, while the fifth and sixth rows correspond to the data shown in Fig. 13.

We note that the taper-microsphere system has a considerable complexity in terms of the supported modes. The taper itself can support a number of transverse modes, and the pump light propagating in each of these can independently couple into a range of sphere modes, with an efficiency determined by an overlap integral (coupling coefficient) for each taper-sphere mode pair. The pump circulating in each sphere mode

Table 1. Details of the Various Experimental Runs Shown in Figs. 12 and 13[a]

Radius [μm]	λ_p [nm]	λ_s [nm]	$\lambda_i^{(0)}$ [nm]	ΔT [μs]	$\Delta\nu$ [MHz]	Q [×10^8]
(i) 180	CH33 [1550.92]	CH47 [1539.77]	1562.30	0.149	3.376	0.56
(ii) 180	CH33 [1550.92]	CH49 [1538.19]	1563.70	0.151	3.374	0.57
(iii) 180	CH34 [1550.12]	CH48 [1538.98]	1561.31	1.630	0.366	5.30
(iv) 180	CH34 [1550.12]	CH49 [1538.19]	1562.70	0.610	0.748	2.50
(v) 135	CH33 [1550.92]	CH48 [1538.98]	1562.70	0.208	2.370	0.825
(vi) 135	CH33 [1550.92]	CWDM [1530]	Not defined	Not defined	Not defined	Not defined

[a]For each run we indicate the microsphere radius, the pump wavelength, the signal photon wavelength, the value of the idler wavelength selected for displaying the TED, the width of the temporal distribution ΔT, the resulting bandwidth of the heralded idler photon, and the associated Q parameter. Rows (i)–(iv) correspond to Fig. 12, while (v) and (vi) correspond to Fig. 13.

then generates photon pairs propagating in turn in a range of sphere modes as determined by the intramode phase-matching properties [see Eq. (8)]. These photon pairs then couple back to the taper, again in accordance with the specific coupling coefficients for each sphere-taper mode pair. We point out that this description must then be applied to each pump frequency (rastered to eliminate thermal effects; see above), within the resonance bandwidth.

Note that while our theory includes the possible contribution of multiple sphere modes, and could be amended to include multiple taper modes each coupling to a collection of sphere modes, in our numerical simulations we assume, for simplicity, a single-sphere mode participating in the SFWM process. Since we cannot at present control which sphere modes contribute to the detected two-photon state in each individual experimental run, an emission bandwidth with a considerable run-to-run variation is likely to result, as is in fact the case.

5. CONCLUSIONS

We have presented a photon pair source based on the SFWM process utilizing a fused silica microsphere as the nonlinear medium. In addition, we have presented a full theory for the SFWM process in these devices that fully takes into account all source characteristics relevant in our experiments. Our theory could be applied also to other types of cavities, such as microrings and microdisks, and predicts all important features of our experimental data including the Q-dependent shape and width of the single-photon frequency comb envelope. As a result of the high optical cavity Q values obtained in our microspheres, heralded single photons with spectral widths down to 366 kHz are demonstrated. This represents a 43× improvement over previous work based on the SFWM process. We have measured SFWM spectra of the generated biphotons, showing pairs of energy-conserving peaks. Filtering a single pair of peaks, we have verified that the SFWM detection rate as a function of the pump power has a quadratic dependence (as expected for the SFWM process) and have shown a well-defined coincidence detection peak as a function of the signal-idler time of detection difference. We have presented a collection of coincidence count measurements as a function of the idler wavelength and the time of detection difference between the signal and idler modes for a given choice of signal-mode spectral transmission window. These measurements represent the emission characteristics of an idler-mode heralded single photon, with the idler emission peaked at the expected energy-conserving wavelength and showing a wide time of detection difference distribution resulting from the cavity-enhanced SFWM process. While the spectral resolution in our measurements is useful to place the spectral peaks to within ∼0.5 nm, we in fact were unable to resolve the extremely narrow spectral widths of individual peaks in the single-photon frequency comb. In this context, we present an effective method for inferring the functional dependence of these individual peaks from an experimental measurement of the time of emission difference distribution. The ultranarrow spectral linewidths made possible by the approach demonstrated here could enable a new set of applications for photon-based quantum information processing.

Funding. Consejo Nacional de Ciencia y Tecnología (1667, 293471, 293694, 376135); Universidad Nacional Autónoma de México (IN104418); Air Force Office of Scientific Research (FA9550-16-1-1458); Universidad de Guanajuato (028/2021).

Acknowledgment. We acknowledge fruitful discussions with Andrea Armani from the University of Southern California.

Disclosures. The authors declare no conflicts of interest.

Data Availability. Data underlying the results presented in this paper are not publicly available at this time but may be obtained from the authors upon reasonable request.

REFERENCES

1. N. Gisin and R. Thew, "Quantum communication," Nat. Photonics **1**, 165–171 (2007).
2. P.-A. Moreau, E. Toninelli, T. Gregory, and M. J. Padgett, "Imaging with quantum states of light," Nat. Rev. Phys. **1**, 367–380 (2019).
3. T. D. Ladd, F. Jelezko, R. Laflamme, Y. Nakamura, C. Monroe, and J. L. O Brien, "Quantum computers," Nature **464**, 45–53 (2010).
4. D. C. Burnham and D. L. Weinberg, "Observation of simultaneity in parametric production of optical photon pairs," Phys. Rev. Lett. **25**, 84–87 (1970).
5. J. E. Sharping, M. Fiorentino, and P. Kumar, "Observation of twin-beam-type quantum correlation in optical fiber," Opt. Lett. **26**, 367–369 (2001).
6. G. Moody, L. Chang, T. J. Steiner, and J. E. Bowers, "Chip-scale nonlinear photonics for quantum light generation," AVS Quantum Sci. **2**, 041702 (2020).
7. Y. Zhao, X. Ji, B. Y. Kim, P. S. Donvalkar, J. K. Jang, C. Joshi, M. Yu, C. Joshi, R. R. Domeneguetti, F. A. S. Barbosa, P. Nussenzveig, Y.

Okawachi, M. Lipson, and A. L. Gaeta, "Visible nonlinear photonics via high-order-mode dispersion engineering," Optica **7**, 135–141 (2020).
8. A. U'Ren, C. Silberhorn, K. Banaszek, I. Walmsley, R. Erdmann, W. Grice, and M. Raymer, "Generation of pure-state single-photon wavepackets by conditional preparation based on spontaneous parametric downconversion," Laser Phys. **15**, 146–161 (2005).
9. J. Liu, J. Liu, P. Yu, and G. Zhang, "Sub-megahertz narrow-band photon pairs at 606 nm for solid-state quantum memories," APL Photon. **5**, 066105 (2020).
10. K. J. Vahala, "Optical microcavities," Nature **424**, 839–846 (2003).
11. X. Ji, F. A. Barbosa, S. P. Roberts, A. Dutt, J. Cardenas, Y. Okawachi, A. Bryant, A. L. Gaeta, and M. Lipson, "Ultra-low-loss on-chip resonators with sub-milliwatt parametric oscillation threshold," Optica **4**, 619–624 (2017).
12. X. Shen, R. C. Beltran, V. M. Diep, S. Soltani, and A. M. Armani, "Low-threshold parametric oscillation in organically modified microcavities," Sci. Adv. **4**, eaao4507 (2018).
13. K. Garay-Palmett, Y. Jeronimo-Moreno, and A. B. U'Ren, "Theory of cavity-enhanced spontaneous four wave mixing," Laser Phys. **23**, 015201 (2012).
14. C. Reimer, M. Kues, L. Caspani, B. Wetzel, P. Roztocki, M. Clerici, Y. Jestin, M. Ferrera, M. Peccianti, A. Pasquazi, B. E. Little, S. T. Chu, D. J. Moss, and R. Morandotti, "Cross-polarized photon-pair generation and bi-chromatically pumped optical parametric oscillation on a chip," Nat. Commun. **6**, 8236 (2015).
15. M. Kues, C. Reimer, P. Roztocki, L. R. Cortés, S. Sciara, B. Wetzel, Y. Zhang, A. Cino, S. T. Chu, B. E. Little, D. J. Moss, L. Caspani, J. Azaña, and R. Morandotti, "On-chip generation of high-dimensional entangled quantum states and their coherent control," Nature **546**, 622–626 (2017).
16. E. Pomarico, B. Sanguinetti, N. Gisin, R. Thew, H. Zbinden, G. Schreiber, A. Thomas, and W. Sohler, "Waveguide-based OPO source of entangled photon pairs," New J. Phys. **11**, 113042 (2009).
17. X. Guo, C.-L. Zou, C. Schuck, H. Jung, R. Cheng, and H. X. Tang, "Parametric down-conversion photon-pair source on a nanophotonic chip," Light Sci. Appl. **6**, e16249 (2017).
18. J. Fürst, D. Strekalov, D. Elser, A. Aiello, U. L. Andersen, C. Marquardt, and G. Leuchs, "Quantum light from a whispering-gallery-mode disk resonator," Phys. Rev. Lett. **106**, 113901 (2011).
19. M. Förtsch, J. U. Fürst, C. Wittmann, D. Strekalov, A. Aiello, M. V. Chekhova, C. Silberhorn, G. Leuchs, and C. Marquardt, "A versatile source of single photons for quantum information processing," Nat. Commun. **4**, 1818 (2013).
20. D. Höckel, L. Koch, and O. Benson, "Direct measurement of heralded single-photon statistics from a parametric down-conversion source," Phys. Rev. A **83**, 013802 (2011).
21. K.-H. Luo, H. Herrmann, and C. Silberhorn, "Temporal correlations of spectrally narrowband photon pair sources," Quantum Sci. Technol. **2**, 024002 (2017).
22. D. Grassani, S. Azzini, M. Liscidini, M. Galli, M. J. Strain, M. Sorel, J. Sipe, and D. Bajoni, "Micrometer-scale integrated silicon source of time-energy entangled photons," Optica **2**, 88–94 (2015).
23. S. Rogers, D. Mulkey, X. Lu, W. C. Jiang, and Q. Lin, "High visibility time-energy entangled photons from a silicon nanophotonic chip," ACS Photon. **3**, 1754–1761 (2016).
24. J. A. Jaramillo-Villegas, P. Imany, O. D. Odele, D. E. Leaird, Z.-Y. Ou, M. Qi, and A. M. Weiner, "Persistent energy–time entanglement covering multiple resonances of an on-chip biphoton frequency comb," Optica **4**, 655–658 (2017).
25. S. F. Preble, M. L. Fanto, J. A. Steidle, C. C. Tison, G. A. Howland, Z. Wang, and P. M. Alsing, "On-chip quantum interference from a single silicon ring-resonator source," Phys. Rev. Appl. **4**, 021001 (2015).
26. X. Lu, W. C. Jiang, J. Zhang, and Q. Lin, "Biphoton statistics of quantum light generated on a silicon chip," ACS Photon. **3**, 1626–1636 (2016).
27. X. Lu, Q. Li, D. A. Westly, G. Moille, A. Singh, V. Anant, and K. Srinivasan, "Chip-integrated visible–telecom entangled photon pair source for quantum communication," Nat. Phys. **15**, 373–381 (2019).
28. J. W. Silverstone, R. Santagati, D. Bonneau, M. J. Strain, M. Sorel, J. L. O'Brien, and M. G. Thompson, "Qubit entanglement between ring-resonator photon-pair sources on a silicon chip," Nat. Commun. **6**, 7948 (2015).
29. L. Caspani, C. Reimer, M. Kues, P. Roztocki, M. Clerici, B. Wetzel, Y. Jestin, M. Ferrera, M. Peccianti, A. Pasquazi, L. Razzari, B. E. Little, S. T. Chu, D. J. Moss, and R. Morandotti, "Multifrequency sources of quantum correlated photon pairs on-chip: a path toward integrated quantum frequency combs," Nanophotonics **5**, 351–362 (2016).
30. Y. Moreno Jeronimo, S. Rodriguez-Benavides, and A. B. U'Ren, "Theory of cavity-enhanced spontaneous parametric downconversion," Laser Phys. **20**, 1221–1233 (2010).
31. P. B. Scott, B. Katja, H. Franklyn, J. Vahala, and S. A. Diddams, "Microresonator frequency comb optical clock," Optica **1**, 10–14 (2014).
32. T. E. Drake, T. C. Briles, J. R. Stone, D. T. Spencer, D. R. Carlson, D. D. Hickstein, Q. Li, D. Westly, K. Srinivasan, S. A. Diddams, and S. B. Papp, "Terahertz-rate Kerr-microresonator optical clockwork," Phys. Rev. X **9**, 031023 (2019).
33. M. Teich, B. Saleh, F. N. C. Wong, and J. H. Shapiro, "Variations on the theme of quantum optical coherence tomography: a review," Quantum Inf. Process. **11**, 903–923 (2012).
34. A. Graciano, P. Y. Martínez, D. Lopez-Mago, G. Castro-Olvera, M. Rosete-Aguilar, J. Garduño-Mejía, R. R. Alarcón, H. C. Ramírez, and A. B. U'Ren, "Interference effects in quantum-optical coherence tomography using spectrally engineered photon pairs," Sci. Rep. **9**, 8954 (2019).
35. Y. Wang, J. Li, S. Zhang, K. Su, Y. Zhou, K. Liao, S. Du, H. Yan, and S.-L. Zhu, "Efficient quantum memory for single-photon polarization qubits," Nat. Photonics **13**, 346–351 (2019).
36. G. Schunk, U. Vogl, D. V. Strekalov, M. Förtsch, F. Sedlmeir, H. G. Schwefel, M. Göbelt, S. Christiansen, G. Leuchs, and C. Marquardt, "Interfacing transitions of different alkali atoms and telecom bands using one narrowband photon pair source," Optica **2**, 773–778 (2015).
37. F. Wolfgramm, Y. A. de Icaza Astiz, F. A. Beduini, A. Cere, and M. W. Mitchell, "Atom-resonant heralded single photons by interaction-free measurement," Phys. Rev. Lett. **106**, 053602 (2011).
38. M. Rambach, A. Nikolova, T. J. Weinhold, and A. G. White, "Sub-megahertz linewidth single photon source," APL Photon. **1**, 096101 (2016).
39. Z. Ou and Y. Lu, "Cavity enhanced spontaneous parametric down-conversion for the prolongation of correlation time between conjugate photons," Phys. Rev. Lett. **83**, 2556–2559 (1999).
40. O. Slattery, L. Ma, P. Kuo, and X. Tang, "Narrow-linewidth source of greatly non-degenerate photon pairs for quantum repeaters from a short singly resonant cavity," Appl. Phys. B **121**, 413–419 (2015).
41. J. Fekete, D. Rieländer, M. Cristiani, and H. de Riedmatten, "Ultranarrow-band photon-pair source compatible with solid state quantum memories and telecommunication networks," Phys. Rev. Lett. **110**, 220502 (2013).
42. D. Grassani, A. Simbula, S. Pirotta, M. Galli, M. Menotti, N. C. Harris, T. Baehr-Jones, M. Hochberg, C. Galland, M. Liscidini, and D. Bajoni, "Energy correlations of photon pairs generated by a silicon microring resonator probed by stimulated four wave mixing," Sci. Rep. **6**, 23564 (2016).
43. S. D. Rogers, A. Graf, U. A. Javid, and Q. Lin, "Coherent quantum dynamics of systems with coupling-induced creation pathways," Commun. Phys. **2**, 95 (2019).
44. P. Imany, J. A. Jaramillo-Villegas, O. D. Odele, K. Han, D. E. Leaird, J. M. Lukens, P. Lougovski, M. Qi, and A. M. Weiner, "50-GHz-spaced comb of high-dimensional frequency-bin entangled photons from an on-chip silicon nitride microresonator," Opt. Express **26**, 1825–1840 (2018).
45. M. Cai, O. Painter, and K. J. Vahala, "Observation of critical coupling in a fiber taper to a silica-microsphere whispering-gallery mode system," Phys. Rev. Lett. **85**, 74–77 (2000).
46. S. Soltani, V. M. Diep, R. Zeto, and A. M. Armani, "Stimulated anti-stokes Raman emission generated by gold nanorod coated optical resonators," ACS Photon. **5**, 3550–3556 (2018).
47. G. P. Agrawal, *Nonlinear Fiber Optics* (Academic, 2007).